Aalto University

OPEN ACCESS

This is an electronic reprint of the original article.
This reprint may differ from the original in pagination and typographic detail.

Iakubivskyi, Iaroslav; Mačiulis, Laurynas; Janhunen, Pekka; Dalbins, Janis; Noorma, Mart; Slavinskis, Andris

Aspects of nanospacecraft design for main-belt sailing voyage

Published in:
Advances in Space Research

DOI:
10.1016/j.asr.2020.07.023

Published: 01/05/2021

Document Version
Peer-reviewed accepted author manuscript, also known as Final accepted manuscript or Post-print

Published under the following license:
CC BY-NC-ND

Please cite the original version:
Iakubivskyi, I., Mačiulis, L., Janhunen, P., Dalbins, J., Noorma, M., & Slavinskis, A. (2021). Aspects of nanospacecraft design for main-belt sailing voyage. *Advances in Space Research*, *67*(9), 2957-2980. https://doi.org/10.1016/j.asr.2020.07.023

This material is protected by copyright and other intellectual property rights, and duplication or sale of all or part of any of the repository collections is not permitted, except that material may be duplicated by you for your research use or educational purposes in electronic or print form. You must obtain permission for any other use. Electronic or print copies may not be offered, whether for sale or otherwise to anyone who is not an authorised user.

Journal Pre-proofs

Mechanical and Thermal Aspects of Nanospacecraft Design for Main-Belt Voyage

Iaroslav Iakubivskyi, Laurynas Mačiulis, Pekka Janhunen, Janis Dalbins, Mart Noorma, Andris Slavinskis

PII: S0273-1177(20)30515-9
DOI: https://doi.org/10.1016/j.asr.2020.07.023
Reference: JASR 14889

To appear in: *Advances in Space Research*

Received Date: 2 February 2020
Revised Date: 17 July 2020
Accepted Date: 18 July 2020

Please cite this article as: Iakubivskyi, I., Mačiulis, L., Janhunen, P., Dalbins, J., Noorma, M., Slavinskis, A., Mechanical and Thermal Aspects of Nanospacecraft Design for Main-Belt Voyage, *Advances in Space Research* (2020), doi: https://doi.org/10.1016/j.asr.2020.07.023

This is a PDF file of an article that has undergone enhancements after acceptance, such as the addition of a cover page and metadata, and formatting for readability, but it is not yet the definitive version of record. This version will undergo additional copyediting, typesetting and review before it is published in its final form, but we are providing this version to give early visibility of the article. Please note that, during the production process, errors may be discovered which could affect the content, and all legal disclaimers that apply to the journal pertain.

© 2020 COSPAR. Published by Elsevier Ltd. All rights reserved.

Journal Pre-proofs

Mechanical and Thermal Aspects of Nanospacecraft Design for Main-Belt Voyage

Iaroslav Iakubivskyi[a,*], Laurynas Mačiulis[b], Pekka Janhunen[c], Janis Dalbins[a], Mart Noorma[a], Andris Slavinskis[d,a]

[a] *Tartu Observatory, University of Tartu, Observatooriumi 1, 61602,Tõravere, Estonia, iaroslav.iakubivskyi@ut.ee, janis.dalbins@ut.ee, mart.noorma@ut.ee*
[b] *Antanas Gustaitis Aviation Institute, Linkmenu str. 28, 08217 Vilnius, Lithuania laurynas.maciulis@vgtu.lt*
[c] *Finnish Meteorological Institute, Erik Palménin aukio 1, P.O. Box 503, FI-00101, Helsinki, Finland, pekka.janhunen@fmi.fi*
[d] *Department of Electronics and Nanoengineering, Aalto University School of Electrical Engineering, Maarintie 8, Espoo 02150, Finland, andris.slavinskis@aalto.fi*

Abstract

We present a detailed mechanical and thermal analysis of a stand-alone nanospacecraft that performs asteroid flybys in the main asteroid belt (2.75 AU) and one Earth flyby at the end of the mission to return the gathered data. A fleet of such nanospacecraft (<10 kg) has been proposed as part of the Multi-Asteroid Touring mission concept, a nearly propellantless mission where the electric solar wind sail (E-sail) is used for primary propulsion. The fleet makes flybys of thus far poorly characterised asteroid populations in the main belt and downlinks scientific data during the returning Earth flyby. The spacecraft size is close to a three-unit cubesat with a mass of less than 6 kg. The spacecraft is designed for a 3.2-year round trip. A 20-km-long E-sail tether is used. A remote unit is attached to the tether's tip and stowed inside the spacecraft before the E-sail commissioning. The remote unit is slightly smaller than a one-unit cubesat with a mass of approximately 750 g. With an electrospray thruster, it provides angular momentum during tether deployment and spin-rate management while operating the E-sail. The selection of materials and configurations is optimised for thermal environment as well as to minimise the mass budget. This paper analyses the main spacecraft and remote-unit architectures along with deployment and operation strategies from a structural point of view, and thermal analysis for both bodies.

Keywords: Nanospacecraft, E-sail, deep-space cubesat, structural design, thermal design

*Corresponding author
URL: iaroslav.iakubivskyi@ut.ee (Iaroslav Iakubivskyi)

Journal Pre-proofs

Acronyms

AOCS Attitude and Orbit Control System. 8, 14, 16, 20, 21, 28, 32, 33, 38–41

AU Astronomical Unit. 4, 6, 8, 9, 16–18, 27, 31, 34, 35, 41

BOL Beginning Of Life. 18, 20

CDP Coulomb Drag Propulsion. 6, 20, 40

DSN Deep Space Network. 4, 39

E-sail Electric solar wind sail. 5, 6, 8–13, 15, 16, 18, 20–23, 27, 31, 33, 38–41

EOL End Of Life. 18, 30

ESA European Space Agency. 6, 16, 18, 39

LEO Low Earth Orbit. 14, 20, 23

MAB Main Asteroid Belt. 4, 5, 8, 9, 30

MAT Multi-Asteroid Touring. 3–10, 13, 17–19, 22–24, 26, 30, 39, 41

MLI Multi-Layer Insulation. 28–30, 32, 34–36, 41

MS Main Spacecraft. 9–13, 15–17, 19, 21, 23–25, 27–34, 38–41

PCB Printed Circuit Board. 28–30, 35

RU Remote Unit. 6–16, 18, 20, 21, 23–28, 30, 34–41

RW Reaction Wheel. 9, 20–22, 31, 41

SPENVIS Space Environment Information System. 16–18

TID Total Ionising Dose. 16, 17

TRL Technology Readiness Level. 7, 31, 37–39, 41

Journal Pre-proofs

Journal Pre-proofs

1. Introduction

Nanosatellites, such as cubesats, became fashionable in the fields of space science and technology during the last decade, with more than 1200 units[1] launched into orbit, as of the year 2020 (Kulu, database 2020). Their architecture provides the opportunity to build hardware in a short period of time with a relatively low budget. The launch cost per unit is relatively low due to their small mass and size, which allows them to share a ride as a secondary payload on a launch vehicle. Compared with bigger ancestors, nanosatellites also ensure a reduced appetite for power, with less, more efficient and miniaturised on-board systems. They have enabled broad access to space (Crusan and Galica, 2019), especially for developing and emerging space nations (Woellert et al., 2011).

The cubesat began its path as a suitable platform for cutting-edge educational projects and technology demonstration. Besides their educational, commercial and, perhaps, military uses, lately they have become sufficiently mature to conduct scientific experiments (Rose et al., 2012). While a cubesat cannot replace a large science mission, it can increase the quality of scientific data by providing additional multi-point measurements and by taking higher risks (Poghosyan and Golkar, 2017).

According to Poghosyan and Golkar (2017), scientifically viable cubesats are classified into five main categories based on the primary mission objectives, where supportive deep-space missions play an important role. In deep space, cubesats can be used for exposure experiments, Earth and astronomical observations, close study of the Moon and its far side, exploration of small bodies (asteroids and comets) as well as Jovian and Saturnian systems. The cubesat-based exploration of asteroids has gained a lot of attention lately (Kohout et al., 2018; Lasagni Manghi et al., 2018; Machuca et al., 2019; Benedetti et al., 2019). Furthermore, interplanetary cubesats, such as ones evaluated in this study, tend to be very suitable for prospecting and reconnaissance missions (e.g., surface mapping, trajectory reconstruction, composition characterisation), and as an intermediate step towards in-situ sampling and processing (Zacny et al., 2016). They provide valuable scientific return at a higher risk, which can be reduced by working in a fleet formation. A fleet of spacecraft, which is considered for the Multi-Asteroid Touring (MAT) mission (Slavinskis et al., 2018), also provides multi-point measurement capability. The miniature instrumentation was lately adapted for cubesat-like satellites. Among such instruments are: spectrometers (Gibson, 2019; Bender et al., 2018; Mason et al., 2020), infrared and microwave sounding systems (Li et al., 2019), particle telescopes (Oleynik et al., 2020), long-duration microgravity platforms (Jarmak et al., 2019), bolometers (Swartz et al., 2019), magnetometers and more advanced lab-on-chip systems (Nascetti et al., 2019). All in all, currently available space instruments are sufficiently suitable for deep-space cubesat-based science experiments (Imken et al., 2017).

[1] Includes individually flying cubesats with volumes ranging from a quarter to twelve units, where one unit is a 10 cm cube, in any orbit except the suborbital flights.

Journal Pre-proofs

In the current study, we employ a Cassegrain-type mapping telescope for our mission; the prototype was built by Pajusalu and Slavinskis (2019).

Nevertheless, designing and developing an interplanetary cubesat remains a pioneering field, especially for teams that are not associated with large space agencies. Some of the new challenges are: power production, communication, navigation, autonomy and, most critically, propulsion (Lemmer, 2017). In addition, a spacecraft platform must comply with thermal and radiation requirements, withstand a long mission duration, as well as fit within limited mass and volume budgets. We suggest that these, and other aspects, have to be evaluated and understood in detail by the community before the first interplanetary nanospacecraft take-off. Recently, the *MarCO* mission with two cubesats has performed independent interplanetary operations (Schoolcraft et al., 2017), and more missions are planned by large space agencies (Crusan and Galica, 2019; Michel et al., 2018), which are relying on the support of Deep Space Networks (DSNs) and/or mothercraft. However, stand-alone cubesats are not studied in detail due to their limited propulsion, communication and navigation capabilities.

Here we present design aspects of a platform for a stand-alone interplanetary nanospacecraft, and configurations for hosting all necessary subsystems and an optical instrument with a minimal mass footprint. The platform is analysed for operations in hot (at 1 Astronomical Unit (AU)) and cold (at 2.75 AU) environments. The nanocraft is customised for the MAT mission, which is described in Section 2. The spacecraft requirements are listed in Section 3. Section 4 provides information about the spacecraft architecture and configurations. Design decisions and analyses are presented in Section 5. The discussion and future work are outlined in Section 6. The conclusions are reached in Section 7.

2. Multi-Asteroid Touring

Small Bodies Assessment Group recommends[2] a balanced program of telescopic observation (ground-based, airborne and space-based), laboratory studies, theoretical research and missions to Main Asteroid Belt (MAB) utilising the full spectral range from ultraviolet to far-infrared to investigate next outstanding fundamental questions in the decade 2023–2032: (i) physical properties and processes, (ii) chemical composition and (iii) evolution and dynamical evolution (McAdam et al., 2020).

Small carbon-rich bodies in the Solar System are challenging to characterise with ground-based or even space telescopes (Carry, 2018). Fewer than 20 out of several hundreds of thousands of known asteroids have been visited by spacecraft so far. For hitherto unstudied objects, a flyby mission (in synergy with remote observations) is the most cost-effective method for gaining knowledge about basic composition, general shape, morphology, regolith cover and activity of an asteroid. Small body science is a complex but important subject that provides

[2]Expressed in the 2020 White Paper (McAdam et al., 2020).

Journal Pre-proofs

knowledge about the formation and evolution of our Solar System and, for instance, origin of water and life on Earth. Many aspects of this science and its importance were recently covered in the special issue of this journal (Palomba and Shea, 2018). A classic mission to small solar system bodies can study 1–2 objects in detail, or flyby many more (i.e., the Lucy mission) (Clark et al., 2018; Snodgrass et al., 2018; Bowles et al., 2018). The objective of MAT is to study a large number of asteroids and, in prominent and risky cases, active asteroids and main belt comets, and how measured composition, shape, morphology, regolith cover and activity vary between them. A fleet is required for that (Slavinskis et al., 2018), however, to make it affordable, the individual spacecraft should be small, for instance cubesat-sized.

MAT is a mission concept dedicated to a distributed close-range spectral survey of hundreds of asteroids by a fleet of nanospacecraft. While the mission is designed to use Electric solar wind sail (E-sail) propulsion in the simplest single-tether configuration, it would significantly improve statistics of the number of visited asteroids with resolved surfaces. The "statistically significant" number of visited asteroids is set between 10 (absolute minimum) and 100 (desired number) from many spectral types and families (ESA, technical report 2018). Each spacecraft is equipped with a miniature monochrome and spectral imager[3] and is designed to visit six asteroids on average (Slavinskis et al., 2018), where one target is primary and others are auxiliary targets near the trajectory path. One instrument relevant to a flyby mission is an optical camera (the prototype was built by Pajusalu and Slavinskis (2019)). This instrument, along with a framing camera, which also acts as a star tracker, is used for navigational purposes throughout the mission; they track planets and other celestial bodies, estimating the spacecraft's position and commanding the E-sail (Segret et al., 2018). The fleet is formed of approximately 50 stand-alone cubesat-like spacecraft. The total mission duration to the MAB is approximately 3.2 years. The MAT mission philosophy is to connect affordable, small and fast-developing mission concepts (i.e., new space) with deep space.

Two types of tethered satellites are used as active propulsion systems: electrostatic and electrodynamic. Non-conductive tethers such as momentum-exchange tether, space elevator tether, space net/harpoon tether and similar ones are less relevant to our study. The electrostatic tether is thin, conductive and charged. The electrostatically-based propulsion (i.e., E-sail) uses Coulomb force as a form of interaction between the tether and a plasma stream that moves relative to the spacecraft. The two main cases thus far studied are braking in orbit of a planet with ionosphere (the plasma brake) and sailing with the solar wind in interplanetary space. The electrodynamic tether is also conductive and charged, but significantly thicker; it utilises the Lorentz force as a form of interaction between the tether and the magnetic field of a planet. The tether deployment in space is an engineering challenge (Yu et al., 2018), and historically encountered various risks (Huang et al., 2018). Larger class missions, such as *TSS-1*,

[3] From near-ultraviolet to near-infrared.

Journal Pre-proofs

SEDS-1, *PMG*, *SEDS-2*, *TSS-1R*, *TiPS* and *YES2*, have successfully deployed up to 20-km-long tethers (Carroll and Oldson, 1995; Levin, 2007; Kruijff and van Der Heide, 2009). The nanosatellite-class mission *KUKAI* has deployed a short tether in space (Nohmi, 2009). However, the deployment of the tether with a diameter under 100 μm for E-sail operation is a pioneering field. Two cubesats *ESTCube-1* and *Aalto-1* were launched with such tethers (Slavinskis et al., 2015; Khurshid et al., 2014). *ESTCube-1* did not demonstrate the tether deployment. The *Aalto-1* satellite is currently active in orbit as of June 2020, and the tether deployment has not been demonstrated yet. The upcoming missions *ESTCube-2* (Iakubivskyi et al., in press 2019) and *FORESAIL-1* (Palmroth et al., 2019) are planning to deploy few-hundred-meter-long tethers.

The E-sail, a type of Coulomb Drag Propulsion (CDP), is a propellantless propulsion, which involves electrostatic interaction between a multi-wired tether, which is long, thin and electrically charged (Seppänen et al., 2011), and solar wind particles (Janhunen and Sandroos, 2007; Janhunen, 2011). The tether is stretched by a physical mass placed at the tether's tip and a centrifugal force provided by the spacecraft's spin (Toivanen and Janhunen, 2014; Slavinskis et al., 2014). While an increased number of tethers would increase the thrust of the E-sail, the MAT spacecraft is designed as a single-tether system. This most simple of E-sail systems has a total length of approximately 20 km and requires spin-rate management because otherwise the orbital Coriolis effect (Toivanen and Janhunen, 2012) changes the spin rate dramatically when the spacecraft orbits the Sun. The spin rate is controlled by the miniature electric propulsion on the Remote Unit (RU), which is located at the tether's tip; this propulsion can also make minor trajectory adjustments by changing the spin plane orientation. Such a spacecraft's architecture dictates system requirements, which are described in Section 3. The spacecraft mass is limited to 6 kg including the tether and the RU. The RU is designed as a separate, active subsatellite, which assists the E-sail operation.

The orientation of the spin plane can be changed by the E-sail's voltage adjustments. For maximum torque, one could apply voltage during one 180-degree half of the rotation and zero voltage during the other half. The angular velocity of the spin-plane trajectory correction is calculated by Equation 1.

$$\omega = \frac{1}{2 \cdot \pi} \cdot \sqrt{\frac{dF/dr}{k \cdot m}}, \tag{1}$$

where dF/dr is the E-sail thrust per length, which is 250 nN$\cdot$m^{-1} for MAT at 10 kV average voltage at 1 AU, and three times smaller at 3 AU (Janhunen et al., 2010); k is the ratio between the tether tension and E-sail force, which can be as low as 3 for single-tether system at 1 AU, and 9 at 3 AU; m is the RU mass (0.75 kg). It results in approximately 10.9 deg$\cdot$h^{-1} at 1 AU and 3.6 deg$\cdot$h^{-1} at 3 AU, if the spin periods and voltages are constant.

Initially, the MAT mission was proposed to the European Space Agency (ESA) Announcement of Opportunity for "New Science Ideas" (ESA, open call 2016). The mission was selected as one of three candidates and was studied

Journal Pre-proofs

during a dedicated delta session of Small Planetary Platforms at the concurrent design facility (ESA, technical report 2018). The study report provided a comparison with the original proposal and focused on indicating shortcomings and validation feasibility. While the study relied on the high-Technology Readiness Level (TRL) systems, in this paper we propose a possible configuration for the platform that employs novel solutions based on modern miniaturised technologies and defines ones to be developed.

2.1. Mission operation adaptation for mechanical and thermal analyses

The mission profile is shown in Figure 1 in Slavinskis et al. (2018). The mission is divided into six operational modes that represent different environmental conditions. The visualisation of the operation concept is shown in Figure 1.

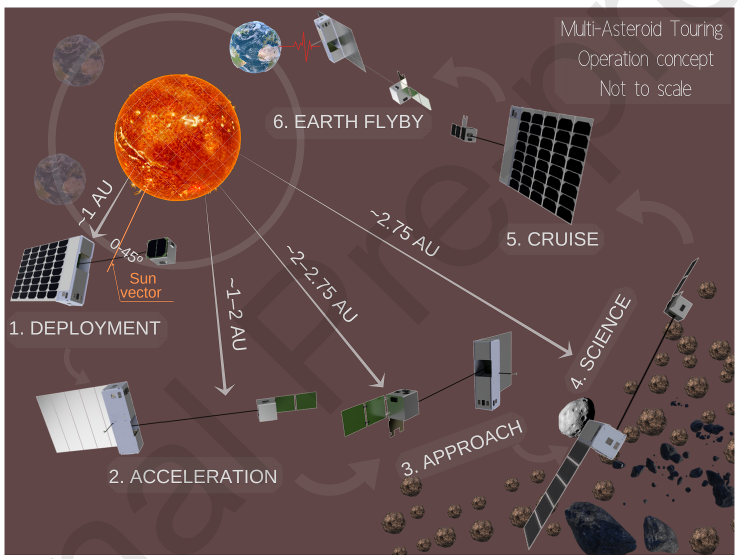

Figure 1: Operational concept of MAT mission.

The main operational modes for pursuing environmental analysis include:

1. Deployment (near the Earth at 1 AU):
    - i) Deployment from a launch vehicle's fairings;
    - ii) Commissioning of spacecraft, detumble, spin-up around a controlled axis and deployment of the RU with the tether;
    - iii) Deployment of solar panels on the RU;
    - iv) Testing low- and high-data-rate communications.
2. Acceleration (1–2 AU):
    - i) Activation of navigation, high-voltage source and electron emitters;

Journal Pre-proofs

ii) Acceleration with the E-sail;

iii) The angle between the spin plane and the Sun is 33.4° at 1 AU and linearly decreases (active control) to 0° at 2 AU;

iv) Low-data-rate communications with the Earth.

3. Approaching the main asteroid belt (2–2.75 AU):

i) Deployment of a thermal screen on the RU;

ii) Active Attitude and Orbit Control System (AOCS) and E-sail manoeuvres to minimise the flyby distance;

iii) Low-data-rate communications with Earth.

4. Science (≈ 2.75 AU)

i) Approaching the target;

ii) Remote sensing during flyby (Pajusalu and Slavinskis, 2019);

iii) Low-data-rate communications with Earth.

5. Cruise (2.75–0.95 AU)

i) Returning back to the Earth's proximity with scientific data stored on board;

ii) Low-data-rate communications with Earth, transmitting the scientific data, if possible.

6. Earth flyby (0.95–1 AU)

i) High-data-rate communications: downlink the scientific data during Earth flyby.

3. Requirements for mechanical and thermal design

In order to fulfil the main science goal to fly by 40 primary targets alongside other requirements from this paper (unless stated otherwise) (Slavinskis et al., 2018), the fleet consists of 40–80 spacecraft (depending on the number of spacecraft per primary target). The requirement for the MAT mission is to transmit at least 20 GB and to store at least 60 GB of science data per spacecraft. Each single-tether 6 kg spacecraft with a 20-km-long tether, which is nominally charged to +15 kV with a peak charge of +30 kV, produces an acceleration of 1 mm·s^{-2} (Slavinskis et al., 2018). In order to reach the MAB within a single heliocentric orbit (approximately 3.2 years), the total spacecraft mass is limited to 6 kg. An increased spacecraft mass would decrease the acceleration[4], and subsequently would significantly increase the mission duration (i.e., more than

[4] 7.5 mN thrust at 1 AU.

one orbit to reach the target) or would require a multi-tether approach, which is an order of magnitude more complex. The spacecraft shall be able to deploy a 20-km-long tether with the centrifugal force. The tether must be attached as close as possible to the satellite's centre of mass. The spacecraft must be able to host an optical instrument (i.e., payload) with a one-cubesat-unit volume. The shape of each spacecraft is not limited, since the fleet is designed as the primary payload, and would require a dedicated launch vehicle.

The primary thermal-control requirement for the MAT mission is to keep the components' temperature within limits (see Table 1) under the widely varying environmental and operational conditions: the relatively warm environment near the Earth and cold conditions in the MAB.

The Main Spacecraft (MS) and RU spacecraft must survive the thermal environment expected during the baseline 3.2-year MAT mission orbit with an aphelion at 2.75 AU, perihelion at 0.95 AU and zero inclination[5]. The operation of the RU during the Earth flyby is not strictly required, as it will not transmit any data or perform spin-plane manoeuvres during this phase.

Components	$T_{operational}$ [°C]	$T_{non-operational}$ [°C]
Battery	0 to +45 charge −20 to +60 discharge	−20 to +50
Main bus	−40 to +85	−40 to +85
TILE propulsion	−10 to +80	−40 to +100
Transmitter	−20 to +50	−40 to +85
Optical instrument	−20 to +60	−40 to +100
Sun sensors	−40 to +100	−40 to +125
Reaction Wheels (RWs) x, y	−40 to +70	—
RW z	−20 to +60	—

Table 1: Component temperature requirements (extreme ranges), where T is temperature.

4. Spacecraft architecture

Each spacecraft in the fleet is designed with a common structural representation. The shape of each spacecraft is built around a three-unit cubesat according to the requirements of modern-design canisterised dispensers with tabs (Tullino and Swenson, 2017).

4.1. Remote unit

The RU is a subsatellite that attaches to the tether tip and is an essential component for the E-sail-spin-rate management and spin-plane control. The

[5]Derived from Slavinskis et al. (2018).

Journal Pre-proofs

initial task of the RU is to deploy the tether and keep it stretched during the entire mission. In previous missions, such as *ESTCube-1* (Slavinskis et al., 2015; Lätt et al., 2014; Envall et al., 2014) and *Aalto-1* (Khurshid et al., 2014), and upcoming missions, such as *ESTCube-2* (Iakubivskyi et al., in press 2019) and *FORESAIL-1* (Palmroth et al., 2019), there was, and will be, an aluminium mass weighing a few grams at the end of the tether serving as a passive RU. In the scope of the MAT mission, the independent operation unit is required in order to control the spin plane and, therefore, to keep the intended trajectory; it also manages the spin rate in order to avoid the orbital Coriolis effect, which influences the spin rate dramatically while orbiting the Sun (Toivanen and Janhunen, 2012). The RU is integrated into the MS in the stowed position and requires deployment for the E-sail operation. Moreover, it must enable critical manoeuvres to reduce the flyby distance at an asteroid. With this in mind, the RU is designed as a small, independent sub-spacecraft whose size is close to one cubesat unit. It hosts a tether with a reel, all necessary subsystems, a battery, deployable solar panels, a deployable thermal screen and electrospray propulsion *TILE-50*, which is discussed in Subsection 4.2.5. High-voltage-supply control boards and electron emitters are located in the MS (see Figure 7) and the tether will be directly attached to it with a slip ring. The slip ring is required in order to avoid tether damage when excessive rotation occurs at either of the tether's ends. The RU design is represented in Figure 2.

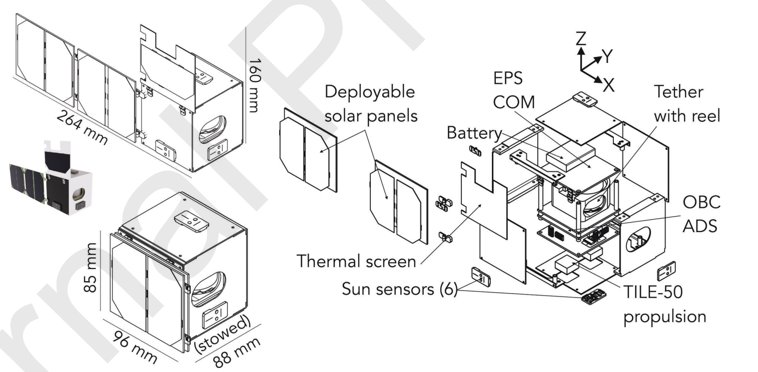

Figure 2: Various views of the RU. The bottom left shows a stowed view, the top left with deployed solar panels and a thermal screen. On the right is an exploded view. EPS – electric power system, COM – communications, OBS – on-board computer, ADS – attitude determination system.

The system is complex and requires the deployment of solar panels and, later, the thermal screen, which protects against overheating at closer distances to the Sun (more details in Subsection 5.2). The opposite side of the thermal screen hosts one more solar cell. The power generation by the RU, calculated with the method described in Subsection 4.2.2, is shown in Figure 3. The deployment of solar panels is enhanced by a centrifugal force, which is already provided by

Journal Pre-proofs

the rotating system[6] for E-sail management around the y-axis. The system's centre of mass (rotation centre) shifts along the tether during RU deployment. The main challenges in the RU design and deployment are:

1. Creating a configuration that balances simple deployment and stowed positioning.

2. Developing a low-force deployment method that will not break the tether during deployment and operation phases (the 35 μm and 50 μm tethers can tolerate a tensile load of approximately 9 cN and 40 cN, respectively).

3. Creating a system which will operate as an independent sub-spacecraft (power generation, simple attitude control, communication with the MS).

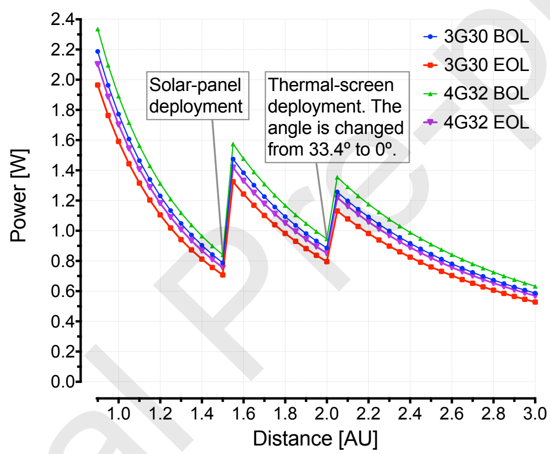

Figure 3: Power production by the RU using various *AzurSpace* solar cells.

Deployment mechanisms of pico- and nanosatellites, typically, use the strain energy of a compressed spring. In the case of RU deployment, it will require a loaded spring in the $+x$ panel in order to push the RU out of the main body. The main difficulties with spring deployment are (i) uncontrolled deployment with a high risk of damaging the tether due to the increased tension, and (ii) an auxiliary tether is required to compensate the tension, which would result in a bounce-back effect with a subsequent risk of collision with the main body that occurs as a result of the acceleration created via deployment. An alternative deployment method would have to be executed with pressurised gas and a piston-like cylinder to create the initial force. This strategy is very similar to the spring-loaded one and, aside from the aforementioned difficulties, adds a pressurised tank with increased volume, mass, cost and complexity. Moreover,

[6]RU and MS around their common centre of mass.

the previous testing of such systems claimed there is an issue with possible uneven force in the sides, which results in tilting (Chahat et al., 2017). The easiest solution is to rely on the centrifugal force, which will require an extended testing campaign. Alternatively, a more sophisticated solution is to use a stepper motor with spur gears sliding on a spur rack, which would provide a controlled translation of the RU (Figure 4). The motor with an external shaft in the tether reel deploys the tether and provides rotation to the drive spur gear. Then the rotation is transferred to the slave spur gear, which provides the translation to the RU with the assistance of the spur rack (fixed to the main body). The spur gear and reel are directly fixed to the same shaft and having the same rotation period. The translation of the RU and tether unreeling are synchronised. It is achieved by the ratio between the outer-tether diameter and slave spur gear being the same as the ratio between the number of teeth (the same pitch) of the drive spur gear and slave spur gear. Further deployment would rely on the centrifugal force.

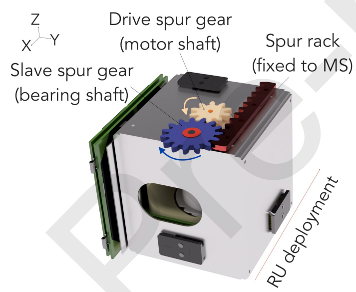

Figure 4: Proposed strategy for RU deployment.

The RU requires communication with the MS in order to control its attitude with respect to the MS. Various manoeuvres are required in order to change the direction of E-sail spin plane in relation to the solar-wind vector and to manage the spin rate. The RU has three degrees of freedom considering the electric propulsion nozzle placement[7]: one translation is in the $+z$ direction and two rotations are around the x-axis. While the stretched tether keeps the RU approximately parallel in the z–y plane, the y–x and z–x planes remain uncontrolled. They will be controlled by activating one of the nozzles in the $-z$-panel, which will provide rotational stabilisation around the x-axis. In order to provide translation in (i) the $+z$ direction, the spacecraft will fire both nozzles, (ii) for the $-z$ direction, the spacecraft will fire one nozzle in order to turn 180°, then stabilise its position, and then fire both nozzles, (iii) for the $-y$ and $+y$ directions, a 90° turn anti- or clockwise will be made with one nozzle fired, the position then stabilised, and then both nozzles fired in order to provide translation in either one of these directions.

[7]Two nozzles apart from the tether's attachment point in $-z$ direction.

The attitude determination and control system is required in order to point the solar panels towards the Sun and to perform the aforementioned manoeuvres for E-sail operation. Attitude control of the RU is accomplished by the electrospray propulsion *TILE-50* and attitude determination by a set of on-board sensors: six sun and four gyroscopic sensors. The information, acquired from sensors, satisfies the requirements from the initial paper (Slavinskis et al., 2018). It is sufficient to perform manoeuvres for E-sail operation and management, in addition to manoeuvres performed by the MS. The information from sensors will be processed by an on-board microcontroller and transmitted to the MS wirelessly. The duty cycle will be low, and the RU will mostly receive commands from the MS for the corrections needed.

4.1.1. Tether

The tether is made out of several thin conductive wires that are bonded together. The previous production technique employed ultrasonic bonding (Seppänen et al., 2013). Currently, the tether is produced in a shape that has a few parallel wires (typically 2–5) and many perpendicular wires resembling rungs in a ladder that creates a multi-cell structure (Envall et al., Presentation at the Sixth International Conference on Tethers in Space 2019, Madrid, Spain). Potential materials for tether production are aluminium, copper alloys, titanium, nickel and steel; previously silver and gold were also considered.

The aluminium tether is preferred for MAT due to low density. A hydrogen bubble formation and sputtering were identified as the potential risks of damaging the tether, however, both effects have a negligible effect during a few-year-long mission. The hydrogen bubble formation is caused by the interaction between the trapped proton and free electron in the aluminium structure (Sznajder et al., 2018). In the course of the sputtering effect, each proton knocks out some aluminium atoms. However, the positive charge of tether would repeal solar protons and only high-energy protons would be able to interact with the tether, in particular solar proton events and galactic cosmic radiation, and the latter has so high energy that would fly through the wire.

Each wire is either 35 μm, 50 μm, 75 μm or 100 μm thick and, if damaged by the micrometeoroid flux, the remaining structure ensures further functionality of the E-sail. The schematics of the tether is shown in Figure 5. The distance between individual wires is illustrative and demonstrates the survivability against micrometeoroids. It also explains the limitation of more-advanced-materials implementation, i.e., carbon nanotubes. Two types of strike probabilities were identified: P_t – an entire tether snap by the large impactor (over 5 cm), P_w – a single tether hit by the impactor from micron to sub-centimetre level. P_w is harmless unless it cumulatively happens enough many times in the same cell and cuts the entire cell P_c. P_t is the least probable and is fatal to any type of space vehicle. The first metre of the tether (attached to MS) would need to be thicker with increased tension-load tolerance in order to minimise the risks associated with the RU deployment. Tethers launched in *ESTCube-1* and *Aalto-1* successfully passed qualification testing (vibrations and shocks); MAT-like tethers are currently tested for *ESTCube-2* and *FORESAIL-1* (Envall et al., Presentation at the Sixth International Conference on Tethers in Space 2019, Madrid, Spain; Iakubivskyi et al., in press 2019).

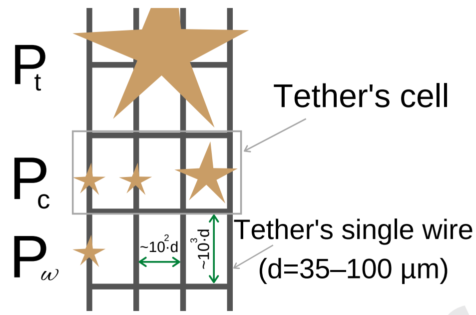

Figure 5: Tether structure and various probabilities to be damaged by micrometeoroids.

The tether-charging process in deep space and ionosphere is similar. The background neutrals are not able to promote arcing because both environments are essentially perfect vacuums: the mean free path of neutral molecules (at least kilometres in Low Earth Orbit (LEO) and much longer in the solar wind) is much longer than the electric sheath radius of the tether. The 19.6-km-long electrodynamic tether was deployed and charged to 3.5 kV during the *TSS-1R* experiment on the Space Shuttle Columbia in 1996 (Stone et al., 1999).

The tether has to fit on the reel and be deployed in space. Two options for the reel design have been considered: permanently housed and jettisonable (ejectable after deployment). A jettisonable reel provides the benefit of a decreased mass of the RU after the tether has been deployed. As a matter of fact, the mass requirement driver is for the satellite in orbit, not the launch mass unit, which does not have a particular limit, in principle. However, the jettisonable system would complicate the deployment mechanism and geometry, as well as the tether attachment. Moreover, it would require additional testing and prior in-orbit demonstration. For this study, a fixed reel inside the RU was selected. It simplifies the geometry and deployment procedure, decreases the probability of failure, and the team has the relevant know-how from the *ESTCube-1* and *Aalto-1* missions. Another factor in the decision-making here is the required surface area for solar cells to generate enough power (i.e., the jettisonable system would occupy some of that surface, however, the current position of solar panels makes an unsymmetrical momentum matrix for AOCS and increases its system cost). Moreover, the reel itself would not be a significant mass contributor, if printed out from *Accura Bluestone* or milled out from *polyether ether ketone* or any other material with low out-gassing and density, and of relatively high strength.

The tether pack size is limited by two factors: the minimum bending radius of the tether and the nested stepper motor size, the latter of which will turn the reel. The selected motor is a *Phytron PhySPACE 19-2*. The stepper motor's outer diameter is 20 mm, which does not limit the bending of the tether. The motor is integrated into a spool with the spool's outer diameter R_S of 26 mm.

The tether pack is created by reeling in a 20 km tether on the spool. Therefore, it creates the radius R_T which dictates the overall dimension of the RU, which in turn dictates the structural cut-out in the MS for RU integration and deployment. The relations between the reel width and the final pack's diameter with various individual wire diameters are shown in Figure 6. The calculation assumed four individual wires with diameters of 35 μm, 50 μm, 75 μm and 100 μm in the tether construction with a packing factor of 1.5 (one-third of the volume is air/vacuum). The optimal width is in the range of 40–60 mm, which makes 35-μm and 50-μm wires in the tether construction suitable for the current RU design.

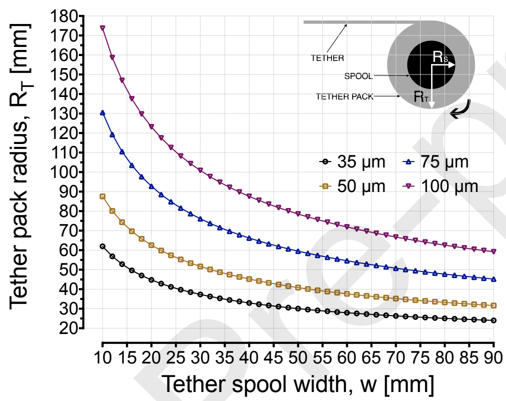

Figure 6: Tether pack R_T formation as a product of tether's wire diameter and the reel width w for the 20-km-long tether.

4.2. Main spacecraft

The MS consists of: (i) telescope assembly (1 kg), (ii) main satellite bus (0.85 kg), (iii) attitude control unit (0.65 kg), (iv) communications module (0.45 kg), (v) RU (0.75 kg) and aluminium tether (0.2–0.6 kg), (vi) deployment systems, such as deployable solar panels (0.6 kg) and feed antenna mechanism (0.1 kg), and (vii) main structure (0.85 kg), see Subsection 4.2.1. The tether mass depends on the thickness of the individual wires, where diameters of 35 μm, 50 μm, 75 μm and 100 μm corresponds to 0.2 kg, 0.3 kg, 0.45 kg and 0.6 kg, respectively.

The aforementioned components with a 35-μm-thick tether result in a total mass of 5.45 kg, which leaves 10% margin. However, the instrument mass might be significantly reduced according to the built prototype (Pajusalu and Slavinskis, 2019) and the main structure might use a thinner wall or use less dense material, if needed. This would allow the use of a 50-μm-thick tether. The visualisation of the MS and its exploded view are shown in Figure 7.

The spacecraft spins around its y-axis in order to provide the centrifugal force for E-sail spin-plane maintenance. The centre of mass of the spacecraft in

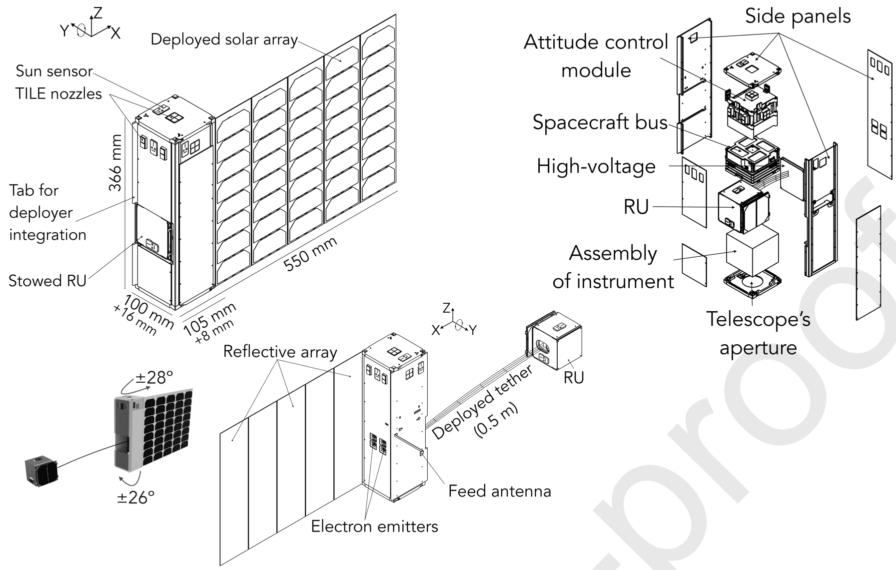

Figure 7: The main spacecraft view from various perspectives.

the stowed position is within 1 cm from the tether axis[8]. Once the solar panels are deployed, the MS's centre of mass shifts along x-axis towards the attachment point of the tether. This results in reduced performance requirements for AOCS and provides the possibility to pitch (rotation around y-axis according to Figure 7) the MS by 26° and roll (rotation around z-axis) it by 28° irrespective of the spin plane. The angular limitation is derived from the avoidance of the tether touching the $-x$ side panel (visualised in Figure 7).

After the deployment of the RU, the entire system's centre of mass shifts along the tether axis away from the MS. The 20 km tether deployment will result in the shift of centre of mass 3.3 km away from the main body, which becomes the centre of the spinning system. The solar panels and E-sail planes are aligned, where the E-sail requires thrust vectoring[9]: it is 33.4° at 1 AU and linearly decreases to 0° at 2 AU.

4.2.1. Outer structure

The increase of the total shielding by the outer structure will result in a mass increase while reducing the Total Ionising Dose (TID) level. The increased wall thickness will also reduce the internal volume of the satellite and limit the size of the internal components. The simulations of TID were implemented by the ESA Space Environment Information System (SPENVIS) *SHIELDOSE-2* model, and the results are shown in Figure 8. The simulations are preliminary and made

[8]Constrained movement along y and z axes.
[9]The angle between the Sun and E-sail plane, which varies between 0 and 45°.

for better assessment of required wall thickness and resulting total mass of the spacecraft at the current study phase. The TID is limited to 26.4 krad with 1-mm-thick aluminium-equivalent shielding, or to 12.3 krad with 2-mm-thick aluminium for the entire mission. The orbital parameters were composed of two segments: (i) a highly elliptical Earth's orbit in order to simulate a single passage (a half-orbit) through the Van Allen radiation belt, and (ii) a circular heliocentric orbit at 1 AU for 3.2 years in order to simulate deep-space travel. While the radiation environment for the second segment is less harmful in practice (in the actual elliptical heliocentric orbit, solar protons will scale down by approximately $r^{-1.5}$, where r is the solar distance (Lario et al., 2007)), the SPENVIS model has a constant proton density for distances larger than 1 AU.

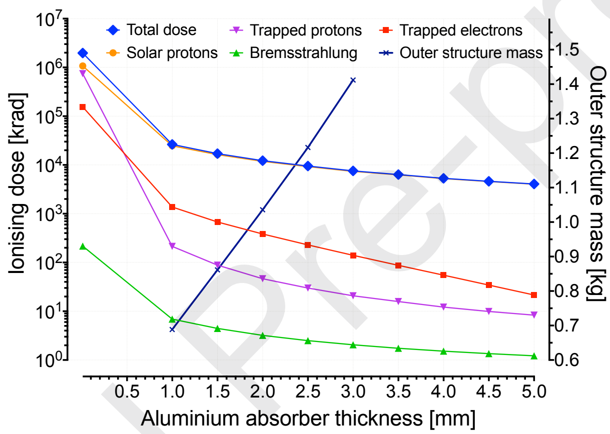

Figure 8: Total ionising dose for the MAT mission and corresponding mass of the MS outer structure.

The wall thickness of 1.5 mm provides a significant drop in TID – by 35% – while the mass increases by 20%. Therefore, this 1.5 mm thickness is recommended for the outer structure with the mass of 0.85 kg, where further decrease of the ionising radiation is possible by the shielding of spacecraft modules and spot shielding of certain components. The detailed radiation analyses shall be performed in the next study phase. The secondary radiation effect shall be evaluated in detail, as in some cases it might be more harmful than a primary source (Dodd et al., 2010).

4.2.2. Power generation and storage

The power on a small satellite is harvested by photovoltaic cells, which are mounted on the body or on deployable panels. Deployable panels are stowed in the dispenser's pockets, which limits the number of panels one can fit without dispenser modifications. There are a few companies, like *DHV Technology*, *OHB Systems* and *Pumpkin Space Systems*, that provide a module with a high number of panels.

The main-body cells are located on the five deployable panels, which are deployed in the $+x$ direction (see Figure 7). Each panel has eight solar cells in a string. The deployment of five folded panels by a three-unit cubesat has not been widely implemented; however it is feasible, since *176 W Pumpkin Deployable Clamshell Solar Arrays* consisting of 22 deployable panels (occupying an entire three-unit volume) have been demonstrated. The deployment strategy will be simplified in comparison with conventional deployment, since the spacecraft will spin around its y-axis for RU deployment, and the resulting centrifugal force will also assist the deployment of panels and maintain their alignment.

The considered cells are *3G30 Triple Junction AzurSpace* and *4G32 Quadruple Junction AzurSpace* cells, providing efficiency of 29.5% and 31.8% at the Beginning Of Life (BOL), respectively. The degradation primarily depends on the thickness of the cover glass and intensity of radiation. Solar cell efficiency also depends on the temperature variations. The low-illumination-intensity environment of equivalent triple-junction cells tested for the Jupiter Icy Moons Explorer mission showed that the efficiency increases from 25% at a room temperature to 33.5% at -150°C (Khorenko et al., 2017). The temperature dependency on the fill factor, which dictates the total efficiency, is linear until -100°C and begins to fluctuate as it gets lower (Khorenko et al., 2017). In a high-radiation environment, the same cells showed a significant degradation in maximum power production in comparison to an open-circuit voltage and a short-circuit current delivery, with a strong recovery effect after exposure (Khorenko et al., 2017; Duzellier et al., 2018). After irradiation with a fluence of 5e14 cm^{-2} 1 MeV electrons at -150°C, the total power varies between 87–94% of the nominal capacity. After room-temperature annealing, this stabilises at 94–96%. While the datasheet of *3G30 Triple Junction AzurSpace* solar cells states a degradation to less than 94% of the absolute value for such a fluence level, for the MAT mission, a degradation to 90% of the nominal capacity was considered. The recommended minimum glass thickness is 100 μm, since this will keep the equivalent electron fluence level below 5e14 cm^{-2} in accordance with the radiation environment, and provide extra margin in the case of potential solar storms. The glass-thickness dependency in the MAT profile is shown in Figure 9, implemented by the ESA SPENVIS *EQFLUX* model.

Thereafter, the efficiency of *3G30 AzurSpace* cells is expected to decrease from 29.5% to 26.5% at the End Of Life (EOL), and for *4G32 AzurSpace* solar cells, from 31.8% to 28.6%. Additionally, the illumination angle will vary, since the solar panels and E-sail planes are aligned, where the E-sail requires thrust vectoring. Hence, the illumination angle of 33.4° and 85% conversion efficiency are used to estimate the power production, which is represented in Figure 10. The illumination angle changes to 0° after the active acceleration with E-sail is completed at approximately 2 AU.

4.2.3. Telescope

The main telescope assembly is the primary scientific payload complemented with a wide-angle framing camera, which also serves as a star tracker. It fits the volume of a one-unit cubesat and the combined mass is less than 1 kg. The

Journal Pre-proofs

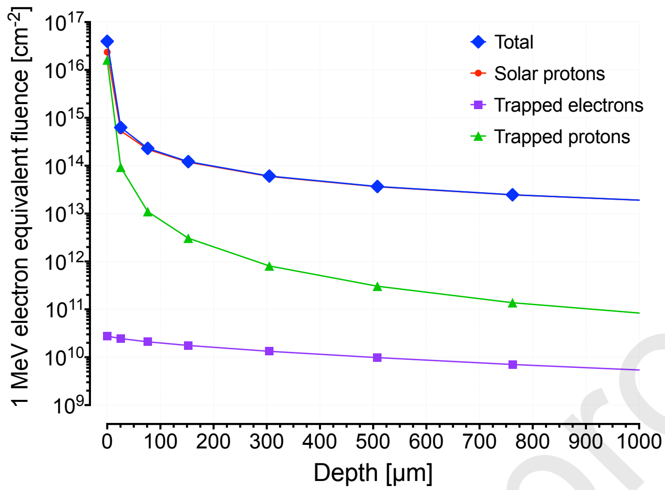

Figure 9: Summary of equivalent fluences in *3G30 AzurSpace* solar cells for the MAT mission profile.

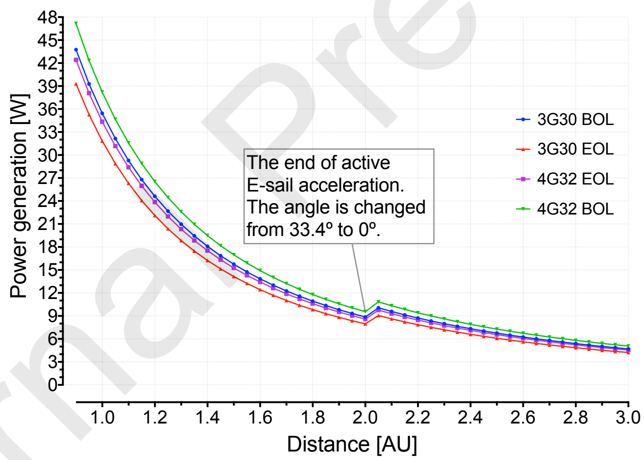

Figure 10: Power generation by the MS with various *AzurSpace* solar cells.

instrument is a Cassegrain-type mapping telescope with a focal length in the range of 135–330 mm and aperture in the range of 4–8 cm. The feasibility of this telescope has been shown previously and the prototype has been developed by Pajusalu and Slavinskis (2019).

The autonomy development will be a major milestone in the MAT mission. The spacecraft requires near-full autonomy since the communications with the ground are brief and rare. The telescope assembly and framing camera will be primarily utilised for this purpose. The synergy between the navigation, imaging scheduling, precision pointing, spacecraft-tether attitude control, power management and thermal control is crucial for scientific objectives fulfilment during the critical asteroid-flyby phase, which will last 25–250 min (target dependant) at a relative velocity of 2–20 km·s^{-1}. These should be accounted for in the autonomy-development phase. The algorithms for cubesat-based absolute navigation has been investigated previously (Knuuttila et al., first view 2020).

4.2.4. Main bus

The main satellite bus design has been adopted from *ESTCube-2*, which has been built as a LEO mission to test the negative CDP for satellite deorbiting and E-sail performance in the ionosphere (Iakubivskyi et al., in press 2019). The bus consists of the electric power system, AOCS, on-board computer, control board for the telescope, RW (*Hyperion RW210*) and eight prismatic batteries (*Panasonic UF103450P*) with a total capacity of 59 Wh (180 Wh/kg) at the BOL. The battery capacity is expected to be reduced by discharge efficiency (0.9) and cycling (0.875), which will result in 44 Wh. While all the bus' subsystems have been developed in-house by the *ESTCube-2* team, further adaptations would be needed to meet the requirements for the deep-space operation. The drawing of the bus is shown in Figure 11.

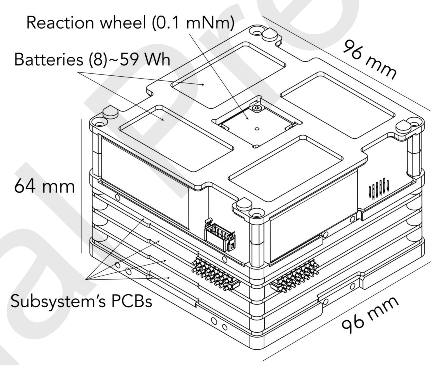

Figure 11: The main satellite bus.

Preliminary system budgets and power equilibrium, which are used for thermal analysis in Section 5, are shown in Table 2. The modes are in accordance with Subsection 2.1. The available power is calculated based on the *4G32 AzurSpace* solar cells (see Subsection 4.2.2).

4.2.5. Attitude control unit

The main objective of the attitude control unit is to spin and point the spacecraft, and maintain the E-sail spin plane. It hosts actuators for the AOCS. The spacecraft requires controlled spin around the y-axis (see Figure 7) in order to deploy the tether and maintain the tension (i.e., stretched) with the assistance of the RU at the tether tip. The spinning system after the deployment will have

Component	Modes power consumption and equilibrium [W]					
	1.Dep.	2.Ac.	3.Ap.	4.Sc.	5.Cr.	6.E. f.
Main Spacecraft						
E-sail	0.1	7–3	3–0.1	0.1	0.1–3	0.1
TILE	1.5	0.5	1.5–0.5	0.5	0.5	0.5
Main bus	0.5	0.5	0.5	0.5	0.5	0.5
Heater	0	0	0–1.6	1.6	1.6–0	0
Transmitter	0.5	0.025	0.5	0.025	0.5	10
Instrument	1	1	1	1	1	1
RW x	0.25	0.5	0.25	0.5	0.25	0.5
RW y	1.05	0.5	0.25	0.5	0.25	0.5
RW z	0.4	0.075	0.1	0.075	0.1	0.1
COM to RU	0.1	0.1	0.1	0.1	0.1	0.1
$\boldsymbol{P}_{output}$	5.4	10.2–6.2	7.2–4.9	4.9	4.9–6.2	13.3
$\boldsymbol{P}_{available}$	37.8	34–8.9	8.5-5.4	5.4	5.4–30.8	30.8
Margin	32.4	23.8–2.7	1.3–0.5	0.5	0.5–24.6	17.5
Remote Unit						
Motor	1	0	0	0	0	0
AOCS	0.1	0.18	0.18–0.1	0.1	0.1–0.18	0.18
Bus	0.2	0.2	0.2–0.1	0.1	0.1–0.2	0.2
Heater	0	0	0–0.25	0.25	0.25–0	0
COM to MS	0.1	0.1	0.1	0.1	0.1	0.1
$\boldsymbol{P}_{output}$	1.4	0.48	0.48–0.55	0.55	0.55–0.48	0.48
$\boldsymbol{P}_{available}$	1.9	1.9–1.08	1.05–0.67	0.67	0.67-4.7	4.7
Margin	0.5	1.42–0.6	0.57–0.12	0.12	0.12–4.22	4.22

Table 2: Subsystems' power budget and power equilibrium at various mission modes. $\boldsymbol{P}$–power, COM–communications.

a spinning period of ∼30 minutes. While the main propulsion system is the E-sail, attitude control of the MS and RU requires an additional propulsion system for attitude and spin-plane control. The E-sail requires Sun vectoring (0–45°) for thrust generation; therefore, the spin plane has to be actively controlled and maintained in a desirable direction (Toivanen and Janhunen, 2012). The relative spin-plane orientation also influences the power generation, which is described in Subsection 4.2.2. Attitude determination is performed by six sun sensors, four gyroscopic sensors, a three-axis accelerometer, and a telescope with a framing camera (which also acts as a star tracker) for navigational purposes (Pajusalu and Slavinskis, 2019). The absolute attitude knowledge required for the mission is 0.1° (Slavinskis et al., 2018). The attitude control is performed by three RWs: (i) one 6 mN·m·s-momentum RW in the z-plane (in accordance with the coordination system in Figure 7), which is embedded into the bus and shown

Journal Pre-proofs

Journal Pre-proofs

in Figure 11, and (ii) two 30-mN·m·s-momentum RWs (*Sinclair Interplanetary RW-0.03*) in the x- and y-planes.

The RWs' desaturation can be achieved by three propulsion systems: (i) cold-gas propulsion (*GomSpace NanoProp 3U*) (Kvell et al., 2014), (ii) ionic liquid electrospray (*Accion System TILE-50*) (Krejci et al., 2017), and (iii) field-emission electric propulsion (*Morpheus Space NanoFEEP*) (Bock and Tajmar, 2018). While all three systems are suitable for MAT's needs (absolute attitude control accuracy of 1° (Slavinskis et al., 2018)), some have strong advantages over others, as pointed out below.

ESTCube-2 uses *GomSpace NanoProp 3U* cold-gas propulsion for attitude control in synergy with a similar satellite bus. However, this propulsion system requires a relatively large storage place for a titanium tank, which is filled with butane and has a capacity ranging from 50 to 100 g (dry mass 300 g) for a three-unit cubesat. It has been shown previously that the customisation of a cold-gas propulsion tank is possible by printing a volumetrically efficient tank (Singhal et al., 2019). The system provides a modular thrust of 1 mN with a 10 μN resolution and a specific impulse of 60–110 s and requires about 2 W of power. The nozzles can be placed around the tank in various directions. The tank has to be kept at 10–20°C in operational mode.

The *TILE* ionic electrospray consists of multiple 1×1 cm^2 emitter arrays bonded to a 1 cm^3 propellant tank (scalable). Each array features 480 emitting tips that are producing thrust in the range of 11–12.5 μN for a 90–172 h operation. The *TILE-50* is capable of producing 50 μN nominal and its specific impulse is 1250 s. The mass of the system is approximately 55 g, it requires up to 1.5 W of power at full thrust and operates at −10 to +80°C. The system is placed on a 3×7×1.2 cm^3 board and is modular in the nozzle-placement arrangements.

The *NanoFEEP* module, TU Dresden spin-off product, is a field-emission electric propulsion that uses gallium (liquid at 30°C) as the propellant and a carbon-nanotube-based neutraliser to avoid electrostatic discharge events, which can cause subsystem damage or failure. A single thruster (maximum thrust of 20 μN) is capable of 1800 h of continuous operation at a low thrust and 400 h at a high thrust; the specific impulse is 3000–8500 s. Eight thrusters with four neutralisers and control electronics have been integrated into the footprint of a one-unit cubesat. Thrusters are modular and can be integrated into rails of a cubesat, while electronics and neutralisers can be placed elsewhere in the satellite. Two thrusters, both with a single neutraliser and electronics, have a combined mass of 160 g (propellant mass 6.5–13 g) and require 0.2–3 W of power. The system has a successful flight heritage.

The MAT concept requires a modular propulsion with a small volume, must operate within a wide temperature range and have a long lifetime; hence, *TILE* and *NanoFEEP* are suitable candidates. While both systems have a similar thrust range with a single thruster, *NanoFEEP* has a significantly longer operational time; however, it is more complex and heavier due to the neutraliser. The E-sail operation requires an electron emitter (neutraliser in *NanoFEEP*) and high-voltage source. Thereafter, the technologies from *NanoFEEP* can be

Journal Pre-proofs

directly implemented in the E-sail hardware. In fact, *ESTCube-2* will use a *NanoFEEP* carbon-nanotube-based neutraliser as the E-sail electron emitter in LEO (Iakubivskyi et al., in press 2019). The decision about the exact system would require thorough attitude control simulation and trajectory analysis, and assessment shall be made in the next study phase when the exact delta-v budget will be known. The required propellant amount and the specific impulse requirement should be derived in order to understand if the systems considered in this section are sufficient for the MS and RU. For this study, it was assumed that the *TILE* system would be used due to its smaller size, and was implemented for the thermal simulation model, which is described in Section 5. The implementation of each system, with 12 nozzles/nozzle arrays, in the MAT architecture is shown in Figure 12. The integration of the *NanoFEEP* or *TILE* systems would require different placement of structural cut-outs, which are comparable by the total area, in the outer structure. However, neither solution would impact the dispenser. The *TILE* system is fitted in the spacecraft as shown in Figure 7.

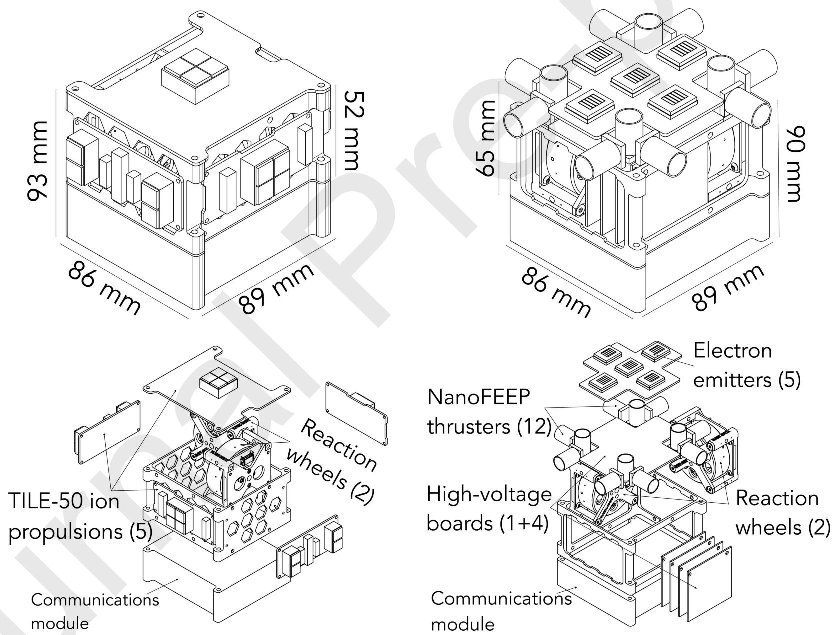

Figure 12: Attitude control module. Top left and bottom left are assemblies of a module powered with *TILE-50* propulsion in stowed and exploded views, respectively. Top right and bottom right are assemblies of a module powered with *NanoFEEP* propulsion in stowed and exploded views, respectively.

4.2.6. Communications approach

During the mission, three types of communication approach are used: (i) low data rate during the entire mission for trajectory updates, housekeeping data monitoring, etc., (ii) high data rate to downlink the scientific data during the

Earth flyby, and (iii) inter-satellite communication between the MS and RU. It is required to transmit at least 20 GB of science data per spacecraft (updated from the previous requirement of 50 GB) and transmit telemetry at 1–60 bit·s^{-1} (Slavinskis et al., 2018).

Low-data-rate communications can be, in principle, executed by a reflective array antenna tuned to X-band with a gain value of 22.5 dBi (Yekan et al., Presentation at the 32nd Annual AIAA/USU Conference on Small Satellites 2018, Logan, UT, USA). A patch antenna was considered, however, it would not provide enough gain to achieve the required telemetry rate[10]. The reflective array is located on the backside of the solar panels; the feed antenna is deployed from the $+y$ side, which is shown on Figure 7. In the worst-case scenario, the spacecraft would require flipping by 180° around the spin axis in order to point the antenna towards Earth, which would subsequently shadow the solar array, and the spacecraft would need to use its battery power. The aforementioned manoeuvre would not damage the tether since it is attached to the high-voltage board with the slip ring. According to the power needs and the capacity of batteries, the satellite could have up to a 2 h window for communications until the batteries would need to be recharged. This requires the nearly fully autonomous operation of the spacecraft. The ground help will take place when verification and status control for on-board autonomy would be needed, especially before the scientific observations. The exact data budget for low-data-rate communications is required in the next study phase.

For communication sessions during the Earth flyby (i.e., high-data-rate communications), use either of a reflective array antenna or a separate X-band patch antenna were considered. The reflective array antenna is the preferable solution due to the capability to downlink more data during the limited flyby time. Thus, the same antenna will be used for low- and high-data-rate communications. Work considering the capability of downlink by MAT spacecraft is ongoing and promising (Dalbins et al., Presentation at the 8th Interplanetary CubeSat Workshop 2019, Milan, Italy).

The communications system requires a dedicated analysis; however, in the scope of this paper, our objective was to verify the hardware feasibility of downlinking 20 GB of science data with existing technology and thermal requirement constraints on the duty cycle. We consider a reflective array antenna on the spacecraft, a 16-m-diameter dish antenna for the ground station receiver (e.g., RT-16 in Irbene, Latvia) and the closest approach to the Earth's centre[11]. The boundary conditions assumed for the link analysis are shown in Table 3.

A classical link equation (Eq. 2) is used to estimate the carrier to noise-density ratio on a decibel scale.

$$\frac{C}{N_o} = EIRP + \frac{G}{T} - (L_{FS} + \sum Other\ Losses) - K\,, \tag{2}$$

[10] 1–60 bit·s^{-1} from Slavinskis et al. (2018).

[11] 10^5–10^4 km, the absolute-position knowledge is 150 km and control is 500 km.

Journal Pre-proofs

Parameter	Value
Carrier frequency	8400 MHz
Transmitter power	33 dBm
Transmitter losses	1 dB
Transmitter antenna gain	22.5 dBi
Antenna pointing error	3 dB
Atmospheric loss	1 dB
Polarisation loss	1 dB
Receiver antenna gain	60 dBi (60% eff.)
Receiver losses	2 dB
Noise temperature of the receiver	58 K

Table 3: Parameters used for the downlink analysis.

where $EIRP$ is the effective isotropic radiated power, G/T is the receiver figure of merit, L_{FS} is the free space path loss, K is the Boltzmann's constant. The bit rate [dBHz] can be expressed in Eq. 3, by assuming that the bit rate [bps] is equal to the noise bandwidth [Hz].

$$R_b = \frac{E_b}{N_o} - \frac{C}{N_o}, \tag{3}$$

where E_b/N_o is the system-required energy-per-bit to noise-density ratio with a link margin included. We consider a binary-phase-shift-keying modulation with a minimum required E_b/N_o of 10 dB and a link margin of 3 dB.

It was found, during successive thermal analyses, that the downlink session time is limited to about seven hours with a 50% duty cycle, after which the maximum allowed transmitter temperature is exceeded (refer to Subsection 5.1.3 for more details). The data rates and associated data throughput during the flyby are shown in Figure 13. The assumed maximum data rate is limited to 100 Mbps, which is an achievable data rate for cubesats; meanwhile, the Planet's *HSD2* system achieves over 1 Gbps in a 0.25U volume (Devaraj et al., 2019).

Two approaches were considered for inter-satellite communications between the MS and RU: (i) to develop low-power wide-area network with communications modules on MS and RU (for instance, *LoRaWAN* and *NB-Fi* (Sinha et al., 2017)), which have available matured solutions for the industry but would require adaptation for space application, (ii) using X-band communications system on the MS coupled with an antenna switch. It would switch from the main reflective array antenna to a one-element X-band antenna (EnduroSat, datasheet 2020). Either solution could fit into the system from a structural point of view. The integration of a one-element X-band antenna into the RU is shown in Figure 14.

4.3. Dispenser

Planetary Systems Corporation provides commercially available dispensers with tabs (Tullino and Swenson, 2017), which provide a number of benefits for

Journal Pre-proofs

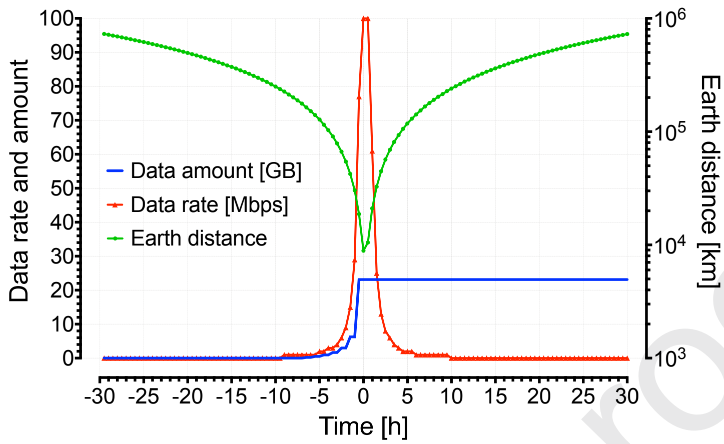

Figure 13: Data rate and downlink of the scientific data starting from the 162^{nd} week of the mission.

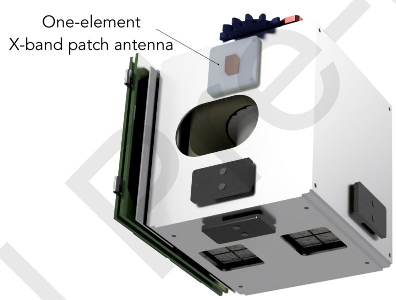

Figure 14: An example of integrating X-band patch antenna into current RU design.

the MAT system: (i) 15% more volume for payload and larger solar-cell strings (i.e., longer structure), (ii) preloaded tabs provide a stiff and jiggle-free load path during the launch, and (iii) increased flexibility with external deployment mechanisms and structural cut-outs. The baseline solution is to employ a three-cubesat-unit dispenser. The maximum spacecraft's mass for this dispenser is 6 kg, which matches the MAT requirement (see Section 3).

Two challenges were identified: (i) stowed volume of five solar panels, and (ii) large gap in one tab due to the RU-related structural cut-out, which is shown in Figure 15. According to the current design and dispenser limitations, we have devoted a pocket volume of $16\times366\times113$ mm^3 for the solar panels. In the opinion of *DHV Technology*, five panels can fit into this volume (Personal communication at the Finnish Satellite Workshop 2020). A payload with non-continuous tabs is allowed by the dispenser provider, however, the large gap (bigger than 25.4 mm) requires a custom dispenser, which would have the same external dimensions. This is a sensible request since the fleet would require a large number of them. Such customisation is common and mentioned in the

Journal Pre-proofs

Journal Pre-proofs

provider's manual.

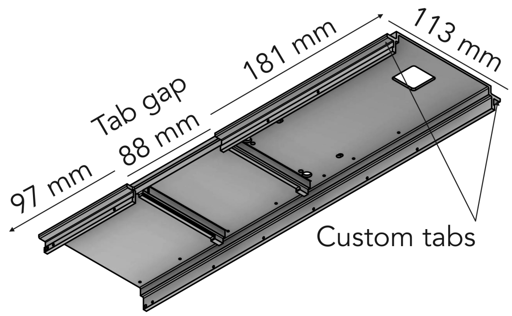

Figure 15: A non-continuous tab layout for the custom dispenser.

5. Thermal analysis and design

Three thermal analysis cases were selected, being the most demanding with respect to the thermal environment:

1. Acceleration from Earth's orbit with the E-sail continuously powered at a maximum thrust (i.e., the high-voltage source running continuously).
2. Spacecraft at the farthest distance from the Sun (2.75 AU) and the minimal expected heat dissipation.
3. Earth flyby with a high-data-rate transmitter downlinking the science data at maximum power.

The first and second cases formed a part of the overall transient thermal analysis of the whole mission orbit. The third case is limited to the Earth-flyby manoeuvre. Both, the MS and the RU, were included in the mission analysis, but only the MS was considered for the flyby case. The operation of the RU during the Earth flyby is not strictly required, as it will not transmit any data or perform spin-plane manoeuvres during this phase. Since the RU and the MS are thermally decoupled, their analyses were performed separately. The thermal modelling and simulations were performed using the *Esatan – Thermal Modelling Suite* software package (*version 2017 sp2*).

5.1. Main spacecraft thermal analysis and design

5.1.1. Thermal-model assumptions

The optical properties used for different surface finishes are shown in Table 4. The values for various surface finishes were taken from Gilmore (2002). The bulk thermal properties used in the model are shown in Table 5. Solar-cell properties were provided by the manufacturer. The main assumptions for the definition of the thermal model are:

Journal Pre-proofs

1. The main body of the spacecraft is made of 1.5-mm-thick aluminium enclosure.
2. Effective emittance of the Multi-Layer Insulation (MLI) (also known as "E-star") is 0.03 based on data from Gilmore (2002).
3. The deployable panels are made from 1.5-mm-thick Printed Circuit Boards (PCBs) with a solar array on one side and a bare glass fibre-reinforced surface on the other side.
4. Each solar-array panel has two hinges represented in the model as 10 $mW \cdot K^{-1}$ conductors.
5. The AOCS and communications subsystem are modelled as aluminium boxes.
6. The spacecraft bus is modelled as a stack of six plates: top aluminium plate, bottom aluminium plate and four PCBs connected to each other with aluminium spacers. Each PCB is modelled as 1.6-mm-thick shell.
7. The battery pack is located between the top plate and one of the PCBs, and it is composed of four boxes in the thermal model, each covered with copper tape.
8. The scientific instrument is modelled as an aluminium enclosure of 1 mm thickness with apertures for the star tracker and the telescope.
9. Thermal contact conductance between the bus and the external structure is 0.1 $W \cdot K^{-1}$.
10. Thermal contact conductance between the external structure and optical instrument is 1 $W \cdot K^{-1}$.
11. The primary and secondary mirrors of the telescope are modelled as 100% reflective in the infrared spectrum.
12. Unused electrical power is dissipated as heat in the solar array.

The main body panels and solar array are meshed with 40×50 mm^2 shells. Each bus PCB is meshed with 32×32 mm^2 shells. The cut-out for the RU is also accounted for in the model and significantly affects the equilibrium temperature. The AOCS has a total of five boards attached on its sides representing the *TILE* propulsion units. The resulting thermal model of the MS is shown in Figure 16. The thermal analysis solution was obtained using the implicit forward–backward difference scheme (the Crank–Nicolson method) with a time step of 1000 s. The boundary conditions used for the analysis are shown in Table 7 and Figure 19. The solar flux is estimated at each 10° of the true anomaly change. In the case where the spin-plane angle with respect to the Sun is not perpendicular, the spacecraft attitude with respect to the Sun constantly changes during a spin period. To account for this variation, at each orbital position the spacecraft is rotated around the spin axis to 12-evenly-spaced angular positions and the resulting solar flux is then averaged. The maximum temperature variation, over the full rotation period of 30 min, is less than 0.9°C and 2°C for internal and external components, respectively. Therefore the averaging does not introduce significant error while greatly reducing the required time for simulations.

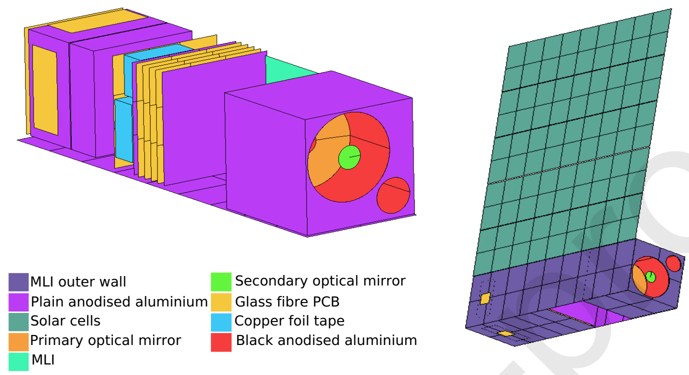

Figure 16: MS thermal model. The internal components are shown on the left and external components on the right.

Material	Emissivity, ϵ	Absorptivity, α
Plain anodised aluminium	0.04	0.26
Black anodised aluminium	0.88	0.88
Copper foil tape, plain	0.02	0.32
Glass fibre PCB	0.89	0.72
Solar cells	0.89	0.91
MLI	0.022	0.14
Mirror (primary and secondary)	0	0
MLI outer wall (teflon)	0.85	0.1

Table 4: Optical properties of various surfaces (Gilmore, 2002).

The modelling of solar-cell optical properties requires special attention. In a steady state (i.e., batteries fully charged) the following energy balance, represented by Eq. 4, applies.

$$W_{em,in} - W_{em,out} - W_{em,dis} - W_{ele,out} - W_{ele,dis} = 0\,, \tag{4}$$

Journal Pre-proofs

Material	Density [kg·cm^{-3}]	Conductivity [W·m^{-1}·K^{-1}]	Specific heat [J·kg^{-1}·K^{-1}]
Aluminium, 7075T6	2810	130	960
Battery	2310	28	900
MLI outer wall (teflon)	1410	0.002	1004
PCB	1850	20	900
Mirror	5323	64	322

Table 5: Bulk thermal properties.

where the energy flow term $W_{em,in}$ is the incident electromagnetic radiation, $W_{em,out}$ is the reflected/irradiated electromagnetic radiation, $W_{em,dis}$ is the absorbed electromagnetic radiation as heat, $W_{ele,out}$ is the electric power used by the subsystems, and $W_{ele,dis}$ is the electric power dissipated as heat. Since the *Esatan* software does not account for the part of absorbed electromagnetic radiation converted to electricity, we intentionally reduce the solar-cell absorptivity by the efficiency of the cells and add the dissipated electrical terms as boundary conditions. The degradation of solar-cell efficiency was not accounted for. Instead, the lowest expected EOL value of 26.5% was assumed (refer to Subsection 4.2.2) for all analysis cases. This is a more conservative estimate from a thermal analysis perspective because reduced cell efficiency increases the heat absorption for the hot case and provides less available power for heaters in the cold case.

5.1.2. Thermal-design choices and simulation results

The goal of this thermal analysis study was to explore the feasibility of attaining thermal requirements using a passive thermal-control approach as much as possible. The MAT mission proposal advocates for a cost-effective deep-space mission with strict mass and therefore volume budgets (Slavinskis et al., 2018); an active control system increases the spacecraft cost and mass, which might disable the reach of the MAB within one orbit (see Section 3). A recent deep-space cubesat *MarCO* utilised two radiators, MLI and heaters for its thermal design (Schoolcraft et al., 2017). This suggests that semi-passive thermal control is a viable approach for an interplanetary cubesat. The thermal design strategy of the MS and RU is to achieve sufficient thermal insulation in order to protect internal components during the cold case, but to leave satisfactory margins for the hot operational case. The design target is to achieve a battery temperature range for charging conditions of 0 to +45°C. This requires a sufficient amount of heating during cold conditions. Adequate thermal insulation is needed in order to compensate for limited electric power. The required thermal insulation was achieved by covering the body with the MLI. In addition, the spacecraft bus and optical instrument are attached to one of the side panels (base plate), which additionally insulates them from the main structure with a thermal resistance of 43.5 K·W^{-1}. The inner surfaces of the structure, which are exposed to deep space after the RU deployment, act as radiators. They

Journal Pre-proofs

require a low-emissivity finish (see Figure 16) in order to reduce the heat loss during the cold case. The properties of plain anodised aluminium have been used for the thermal simulations, alternatively, a layer of gold can be applied.

The minimum and maximum temperatures of the final design are shown in Figure 6. The temperature variations of the MS's components during the entire mission cycle are shown in Figure 17. The internal and external temperature distribution of the spacecraft for hot and cold cases is shown in Figure 18. The results show that all temperature requirements will be satisfied throughout the mission. The E-sail's control electronics and electron emitters reach the temperature of almost -50°C during the cold case. Since the E-sail subsystem is currently at low TRL, an output requirement for this system is to comply with the operational temperature range of -67 to $+82$°C, which includes a 17°C margin (more details in Section 6).

Component	$T_{required}$ [°C]		T_{result} [°C]		T_{margin} [°C]
	MIN	MAX	MIN	MAX	
Battery	-20	$+60$	-0.9	43.4	19.1
On-board computer	-40	$+85$	-4.0	44.2	40.8
Electric power system	-40	$+85$	-3.3	44.6	40.4
Transmitter	-20	$+50$	-7.6	42.4	7.6
E-sail electronics	—	—	-49.8	64.9	—
Optical instrument	-20	$+60$	-10.5	41.9	9.5
Sun sensors	-40	$+100$	-7.6	42.6	32.4
RWs x, y	-40	$+70$	-7.6	42.4	27.6
RW z	-20	$+60$	-0.64	43.4	16.6
TILE thruster	-10	$+80$	-7.6	42.6	2.4

Table 6: Simulated temperatures against the requirements for the MS in the extreme cases.

The solar array of the MS would have to be pointed directly towards the Sun at roughly a 2 AU distance in order to provide enough power for battery heaters, as can be seen in Figure 19. Before that, the solar array can generate enough power at the nominal 33.4° tilt angle without the need for the MS to keep the Sun-pointing attitude during the rotation period. For the E-sail operation, the optimal spin-plane angle with respect to the Sun can vary in the range of 0 to 33.4° during the mission. In the science phase, the maximum angle depends on how precisely one wants to optimise the asteroid flyby distance. This might conflict with thermal requirements. In that case, the spacecraft can move independently of the E-sail up to 26° in pitch and 28° in roll as described in Subsection 4.2. A dedicated study in the next phase is needed in order to verify if this range is sufficient to achieve the scientific objectives.

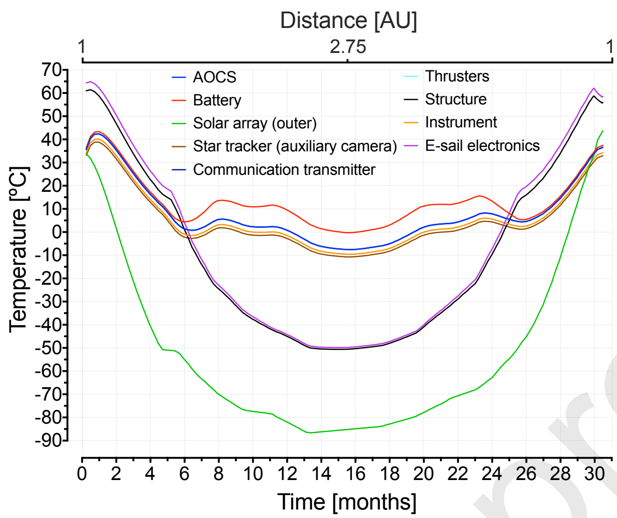

Figure 17: The mean-temperature profile of the MS throughout the mission. AOCS, transmitter and thrusters follow a very close trend. Battery heater activity can be observed from month 6 to 24. The time step is 1000 s, the initial temperature is 0°C.

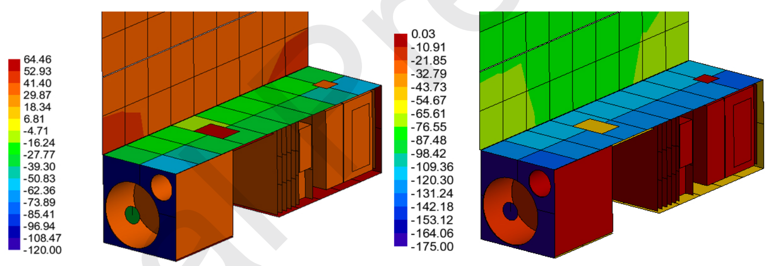

Figure 18: The thermal map of the MS for hot (left) and cold (right) cases (+y side panel is hidden). The temperature scale is in degrees Celsius. Large temperature gradients on the outer cover of the MLI can be explained by the low thermal conductivity of the material and the radiative heat flux from the solar array.

5.1.3. Transient thermal analysis of Earth flyby

For the science data downlink session (see Subsection 4.2.6), a transient thermal analysis case is performed. The flyby distance from the Earth, as well as the orientation of the Sun–Earth line of sight were derived from the preliminary orbital parameters of the mission science study (Slavinskis et al., 2018). The analysis included a period of about 60 days[12] where the distance from the Earth's centre ranged from 10^6 to below 10^4 km. The downlink was initiated about six hours before the closest approach, with a 50% transmitter

[12]Starting from the 162^{nd} week of the mission.

Component	P consumption [W]	P dissipated as heat [W]
Spacecraft bus	0.5	0.5
Transmitter	0–10	0–10
E-sail electronics	0–7	0–3.5
TILE electrospray	0.5	0.5
Optical instrument	1	0
AOCS	1	0.5
Battery heaters	0–1.65	0–1.65

Table 7: Boundary conditions for the MS thermal analysis, where P is power.

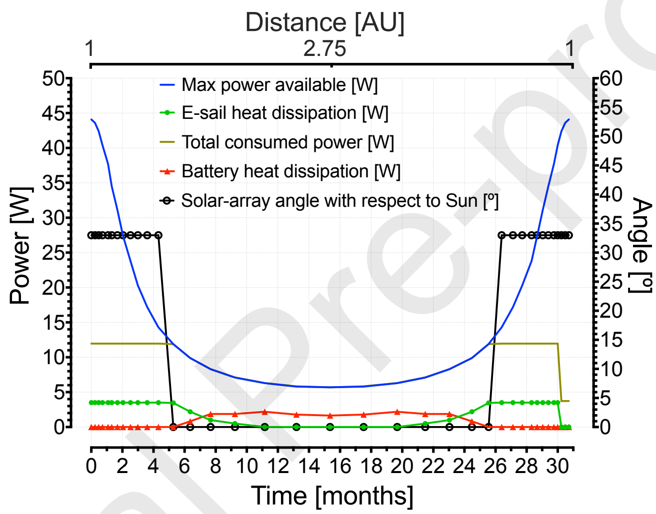

Figure 19: Boundary conditions of the MS. The power available does not account for conversion losses. Attitude angle with respect to Sun is dictated by thermal requirements.

duty cycle[13]. The temperature of the spacecraft subsystems during this period is shown in Figure 20. After about seven hours of downlink time, the transmitter temperature starts to exceed the upper limit of +50°C. During the flyby, the spacecraft attitude was fixed to an Earth-pointing mode. The angle between the solar array and the Sun changes from the initial 70° to 13° by the time of the closest approach. This explains why the spacecraft cools down initially but then heats up immediately after switching on the transmitter. The downlink session can be extended during the journey away from Earth after the system cools down.

[13] 30 minutes on, 30 minutes off.

Journal Pre-proofs

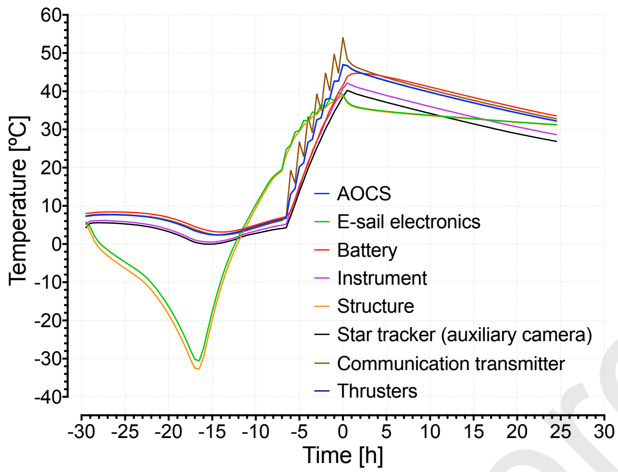

Figure 20: Earth-flyby mean-temperature profiles of the MS. Time "0" corresponds to the closest Earth-flyby distance.

5.2. Remote-unit thermal analysis

The following challenges are associated with thermal control of the RU:

- Negligible power available for heaters of sensitive components during the cold phase of the mission.
- The RU has to be deployed from the inside of the MS; thus the use of MLI for thermal insulation is constrained due to potential interference during the deployment and the limited available surface area.

The thermal-control strategy of the RU is to thermally isolate the avionics board, which also contains a battery, and the *TILE* electrospray propulsion board from the spacecraft structure. To further improve the insulation, we suggest covering the inner spacecraft wall with vapour-deposited gold. To keep the temperatures below the upper limits during the hot phases of the mission, a white paint surface finish is suggested with low absorptivity and high emissivity (see Table 8). In the acceleration phase, the deployment of solar panels can be delayed to create a heat-shield effect. When stowed, the solar array acts as effective multi-layer insulation and reduces the maximum temperature of avionics and propulsion subsystems. The deployment of the array takes place when the spacecraft's distance from the Sun increases and more power is needed to heat up the spacecraft. Initially, two solar panels are deployed at a 1.5 AU distance and the remaining thermal screen is deployed at 2 AU. During the cold phase, patch-resistance heaters are used to keep the temperature of the *TILE* propulsion subsystem and battery above the required minimum limits (see Tables 1 and 2).

The thermal model of the RU is shown in Figure 21. The structure was modelled as a 1-mm-thick enclosure made from aluminium. Each side panel of the enclosure is meshed into 16-lumped-parameter thermal nodes. The electronics boards and solar cells were modelled as PCB shells of 1 mm thickness. PCBs are connected to each other and to RU structure with spacers, which were modelled as thermal conductors attached to corner thermal nodes. The optimal thermal insulation from RU structure is 1 mW$\cdot$K^{-1} and 0.3 mW$\cdot$K^{-1} for propulsion and bus boards, respectively. This is achieved by *polyether-ether-ketone* spacers. The bulk thermal properties are the same as in Table 5.

The analyses show that the temperature environment inside the spacecraft is also sensitive to the outer-surface optical properties and solar-array-hinge conductance. The lowest possible hinge conductance is required to keep the temperatures high enough at 2.75 AU. Unfortunately, we could not find references for hinge conductance in spacecraft. The thermal-contact conductance mechanism in hinges is similar in nature to dry metal bearings, for which values below 10 mW$\cdot$K^{-1} have been reported by Gilmore (2002). By using teflon hinges instead of metal materials, one could reduce the conductance even more. However, a conservative value of 20 mW$\cdot$K^{-1} is used in the analyses.

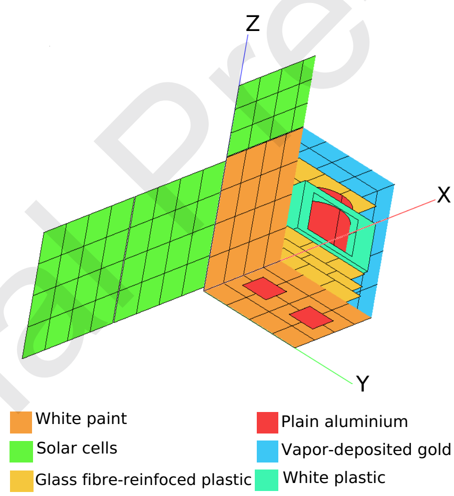

Figure 21: The thermal model of the RU with the fully open solar array. The back side of the solar array is covered with the MLI.

The temperature variations of various components in the RU during the entire mission cycle are shown in Figure 22, and the temperature range with margins in Table 9. The thermal-analysis solution was obtained using the implicit forward–backward differencing scheme (the Crank–Nicolson method) with a time step of 300 s. Boundary conditions of the analysis are shown in Figure 23. It shows the power generated by the solar array, attitude angle with respect to

Material	Emissivity, ϵ	Absorptivity, α
Vapour-deposited gold	0.02	0.19
White paint	0.94	0.07
Solar cell	0.89	0.91
Glass fibre-reinforced plastic	0.89	0.72
Plain aluminium	0.03	0.16
White plastic	0.87	0.39
MLI	0.022	0.14

Table 8: Optical properties of the RU surfaces.

the Sun and internally dissipated power. As can be seen from Figure 22, the spacecraft bus and propulsion subsystems are well isolated from the remaining structure and experience mostly room temperature conditions. This also explains why internal components react very slowly to changes in external heat flux, which is demonstrated by the temperature increase at the initial mission phase. The spikes in temperature correspond to the moment when the deployment of solar panels occurs, causing more heat flux to be absorbed and temperatures to increase.

Component	$T_{required}$ [°C]		T_{result} [°C]		T_{margin} [°C]
	MIN	MAX	MIN	MAX	
Battery	−20	+60	15.4	45.4	14.6
Avionics board	−40	+85	15.4	45.4	39.6
Tether-reel board	−40	+85	7.8	41.7	43.3
Sun sensors	−40	+85	8.1	44.0	41.0
TILE thruster	−10	+80	8.0	46.9	18

Table 9: Simulated temperatures against the requirements for the RU in the extreme cases.

Journal Pre-proofs

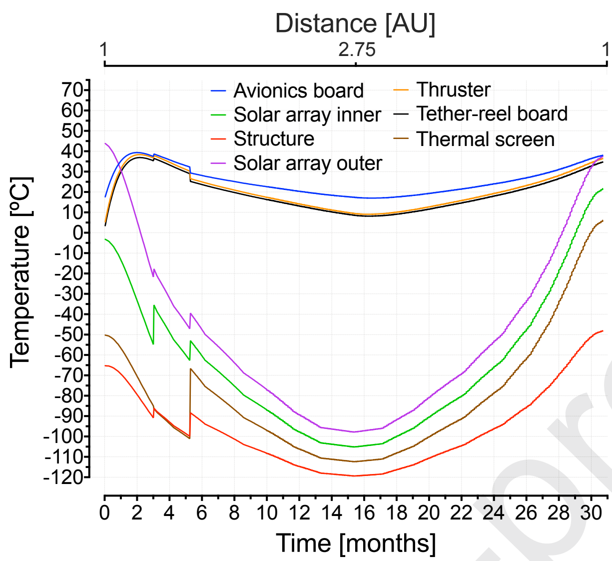

Figure 22: The mean-temperature profile of the RU throughout the mission. The temperature curves of the tether-reel board and thrusters follow a very close trend. The transient-analysis time step is 300 s, the initial temperature is 0°C.

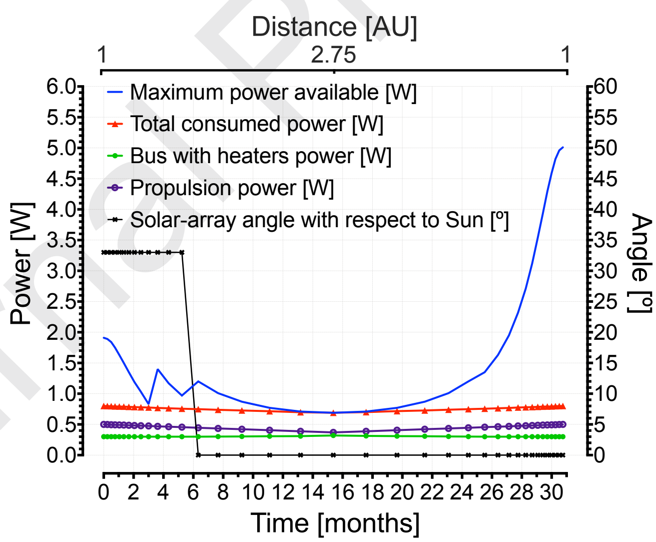

Figure 23: Boundary conditions of the RU.

5.3. Thermal analyses outcome

Based on the current design, we provide temperature requirements for low-TRL subsystems in Table 10. They include a 17°C margin, which is recom-

Journal Pre-proofs

Journal Pre-proofs

mended in the literature (Gilmore, 2002).

Component	T required [°C]	
	MIN	MAX
Main Spacecraft		
On-board computer	-20	$+62$
Electric power system	-20	$+62$
Transmitter	-25	$+60$
E-sail electronics	-67	$+82$
Optical instrument	-28	$+60$
Sun sensors	-25	$+60$
Remote Unit		
Avionics board and battery	-1.6	$+62.4$
Tether-reel board	-9.2	$+58.7$
Sun sensors	-8.9	$+61.0$

Table 10: Temperature requirements for low-TRL subsystems with a 17°C margin. The E-sail electronics include high-voltage board and electron-emitters board.

Based on the simulation results and current design limitations, we can specify the following requirements for spacecraft structure and mission geometry:

1. Required solar-array hinge conductance is 20 mW·K^{-1}. The hinges need to be qualified for a deep-space use.
2. RU's outer surface absorbtivity and emissivity requirements are α=0.07 and ϵ= 0.94, respectively. Space qualification of such surface finish is needed.
3. At certain phases of the mission, both the MS and RU solar arrays must be oriented directly towards the Sun (see Figures 19 and 23). This might negatively affect mission operations and needs to be assessed in more detail.
4. The MS and RU must use higher efficiency solar cells – *4G32 AzurSpace*.

6. Discussion and future work

The RU deployment from the MS is a challenging task and requires the development and testing of such a system. The initial deployment of the RU would require the first meter of the tether to be composed of multiple 100 μm wires (can tolerate over 2 N load), while the rest to be made out of 35-μm-thick wires. The AOCS performance for RU deployment (mechanical load on the tether) shall be assessed in the next study phase. If the mechanical load on the tether would exceed 9 cN, the 50 μm wires should be considered for the tether production. This tether can tolerate approximately a 40 cN load and can fit inside the current design while increasing the total mass by 100 g. The tether

Journal Pre-proofs

must be attached to the high-voltage source with the slip ring. Since the RU might overheat during the return journey, the impact of failure on the E-sail operations must be analysed in detail and consequences evaluated.

The instrument can be pointed to an asteroid without gimbals thanks to the possibility of tilting the spacecraft (26° pitch and 28° roll), irrespective of the phase of the tether's rotation. It is possible by attaching the tether at the MS's centre of mass, as described in Subsection 4.2. The closest flyby of asteroid needs detailed simulations and analysis since the limited manoeuvrability might be constraining for useful science observations. Further instrument development and adaption for nearly autonomous navigation are required.

The orbital parameters, along with the AOCS performance for MS and RU, shall be evaluated in detail. The required propellant amount and the specific impulse requirement should be derived in order to understand if the systems considered in Subsection 4.2.5 are sufficient for the MS and RU. Two novel propulsion systems are proposed in this paper and selection shall be made in the next study phase.

The low- and high-data-rate integrated communications system should be designed with the high-data-rate capability and data-rate adjustability in mind. The required maximum data rate should be evaluated in the next study phase and is mission dependent. To communicate with Earth, a reflective array antenna integrated on the opposite side of the solar array was decided on. The maximum volume for five stowed solar panels is $16\times366\times113$ mm^3, which provides a 366×565 mm^2 area for the reflective array. To reduce costs, only low-data-rate communication sessions would use DSNs services, but high-data-rate communications would use services of physically smaller, cheaper and more available ground stations. The inter-satellite communication system, between the MS and RU, requires assessment, and one of the proposed solutions in Subsection 4.2.6 shall be selected.

If a custom three-cubesat-unit dispenser will become unfeasible in the later phases, for any reason, the six-unit dispenser can be considered for three-unit MAT spacecraft. In this case, the base plate with tabs would need to be customised for the integration (increased width from 113 mm to 239 mm), which will increase the mass of the spacecraft by approximately 250 g. It would also require better thermal isolation of the base plate from internal modules. On the other hand, it will shift the centre of mass closer to the geometric centre, which will greatly benefit the AOCS.

We found that the temperature of components is sensitive to spacecraft attitude, solar-array hinge conductance, power dissipation, and external surface properties. The thermal design, which partly complies with current requirements, is suggested; further improvements during the next study phase are needed. Based on the current design, we provided temperature requirements for low-TRL subsystems in Table 10. We admit that the required temperature range for the E-sail subsystem might be challenging to comply with. A high-power dissipation and specific placement of this subsystem make large temperature excursions. Similar problems have been reported in recent ESA's study on a deep-space cubesat mission (M-ARGO): the heat dissipation from the electric

Journal Pre-proofs

propulsion could be marginally sustained with a passive thermal control (Walker et al., 2018).

The thermal analysis presented here is not conclusive yet. The effect of transient eclipses on battery lifetime needs to be considered during the launch phase, asteroid flyby and in case of an attitude anomaly. A coupled thermal and orbit-optimisation scenario is recommended because the size of the solar array affects both the temperature profile and mass of the spacecraft. If the mass of spacecraft in the next study phase would allow the additional system (i.e., the mass of the telescope assembly might be reduced according to the built prototype by Pajusalu and Slavinskis (2019)), an active thermal control shall be considered. For instance, cubesat-compatible thermal control louvers have been patented and successfully tested in space (Evans, 2019).

The detailed radiation analyses shall be performed and various proposed techniques for radiation protection need implementation (Selčan et al., 2017).

7. Conclusions

The desire to significantly increase the number of imaged asteroids is expressed by various fields of space science. A spacecraft fleet could provide it, but to make it affordable, the individual spacecraft should be small, preferably cubesat-sized. For hitherto unstudied bodies, a flyby mission is the most cost-effective approach, which can be followed by orbiters and landers for the most interesting objects.

This paper demonstrates the design aspects of novel deep-space cubesats, which would form a fleet for main-asteroid-belt flybys. Each 6 kg stand-alone spacecraft is propelled by the Electric solar wind sail (E-sail), a type of Coulomb Drag Propulsion (CDP), with an average mission duration of approximately 3.2 years. Each three-cubesat-unit spacecraft is equipped with the bus, rechargeable batteries, communications transmitter, Attitude and Orbit Control System (AOCS) module (reaction wheels and electric propulsion), telescope, 20-km-long tether, Remote Unit (RU), deployable solar array, and deployable feed antenna. The deployable solar array acts as a power harvester on one side (i.e., covered with solar cells), and as a reflective array antenna on the other. The gathered multispectral and broadband images from asteroids (visual to near-infrared range, covering 400–5000 nm) are downlinked by the antenna during an Earth flyby at the end of the mission. The E-sail's tether is equipped with an independently operated subsatellite (referred to as the RU) at one end and is attached to the spacecraft's high-voltage source. The RU design provides a novel solution for the E-sail management: it is equipped with miniature electric propulsion that assists manoeuvres for the spin-rate control and the spin-plane directional adjustments. The 750-g subsatellite is integrated into the Main Spacecraft (MS) in the stowed position. Its deployment is planned in two steps: first mechanically from the MS and then by a centrifugal force provided by the spinning spacecraft. The tether manufacturing requires the assembly of two pieces: the first meter to be made out of multiple 100 μm wires and the rest – 35 μm or 50 μm wires.

Journal Pre-proofs

Journal Pre-proofs

A custom three-cubesat-unit dispenser with a non-continuous tab (i.e., one tab requires large middle gap, see Subsection 4.3) is needed for the MAT spacecraft. This dispenser would have the same external dimensions as a standard one.

Two propulsion systems for RWs desaturation and two tether diameters have been proposed; selective decisions require a detailed assessment of the Attitude and Orbit Control System (AOCS) during the RU deployment and E-sail operation.

The MS would produce 38 W of power during the closest approach of 0.95 AU, and 5.4 W at the farthest distance of 2.75 AU; the fully deployed RU would produce 4.7 W and 675 mW for the aforementioned conditions, respectively.

The semi-passive thermal design has been proposed based on the combination of MLI, choice of surface optical properties and active heaters. In order to keep the battery within the operational temperature range at 2.75 AU, the required electrical power for heaters is 350 mW and 1.65 W for the RU and MS, respectively. The temperature requirements for low-TRL subsystems have been provided based on the simulation results. It was found that temperatures are sensitive to solar array hinge contact conductance and more research in this field might be necessary to support the results by experimental data. Based on simulations for the Earth flyby scenario, the data-downlink operation is limited to seven hours on a 50% duty cycle until the upper-temperature limit of the high-data-rate transmitter is reached. Considering the limited size of solar arrays and the power budget, the attitude control system is required to point the solar arrays directly towards the Sun: above 2 AU for the MS, and at 2.75 AU for the RU.

Acknowledgements

The authors would like to express their gratitude to Tartu Observatory, Aalto University, the ESTCube team and the Finnish Meteorological Institute for all their help, assistance and guidance. The initial results presented have been achieved under the framework of the Finnish Centre of Excellence in Research of Sustainable Space (Academy of Finland grant number 312356). Conference travel and visiting research to Aalto University were supported by the Archimedes Foundation and an Erasmus+ traineeship grant.

The software for thermal simulations *Esatan* was kindly provided by *ITP Engines UK ltd.*, for the structural design by *Autodesk*, and for priceless communications by *Fleep*.

References

Bender, H.A., Mouroulis, P., Dierssen, H.M., Painter, T.H., Thompson, D.R., Smith, C.D., Gross, J., Green, R.O., Haag, J.M., Van Gorp, B.E., Diaz, E., 2018. Snow and Water Imaging Spectrometer: mission and instrument concepts for earth-orbiting CubeSats. Journal of Applied Remote Sensing 12, 044001. doi:10.1117/1.JRS.12.044001.

Benedetti, G., Bloise, N., Boi, D., Caruso, F., Civita, A., Corpino, S., Garofalo, E., Governale, G., Mascolo, L., Mazzella, G., Quarata, M., Riccobono, D., Sacchiero, G., Teodonio, D., Vernicari, P.M., 2019. Interplanetary CubeSats for asteroid exploration: Mission analysis and design. Acta Astronautica 154, 238 – 255. doi:10.1016/j.actaastro.2018.05.011.

Bock, D., Tajmar, M., 2018. Highly miniaturized FEEP propulsion system (NanoFEEP) for attitude and orbit control of CubeSats. Acta Astronautica 144, 422 – 428. doi:10.1016/j.actaastro.2018.01.012.

Bowles, N., Snodgrass, C., Gibbings, A., Sanchez, J., Arnold, J., Eccleston, P., Andert, T., Probst, A., Naletto, G., Vandaele, A., et al., 2018. CASTAway: An asteroid main belt tour and survey. Advances in Space Research 62, 1998 – 2025. doi:10.1016/j.asr.2017.10.021.

Carroll, J., Oldson, J., 1995. Tethers for small satellite applications, in: Proc. of the 9^{th} Annual AIAA/USU Conference on Small Satellites, Logan, UT, USA. pp. 1–16. URL: https://digitalcommons.usu.edu/smallsat/1995/all1995/38/.

Carry, B., 2018. Solar system science with ESA Euclid. Astronomy & Astrophysics 609, A113. doi:10.1051/0004-6361/201730386.

Chahat, N., Hodges, R.E., Sauder, J., Thomson, M., Rahmat-Samii, Y., 2017. The Deep-Space Network Telecommunication CubeSat Antenna: Using the deployable Ka-band mesh reflector antenna. IEEE Antennas and Propagation Magazine 59, 31–38. doi:10.1109/MAP.2017.2655576.

Clark, B.E., Barucci, M.A., Zou, X.D., Fulchignoni, M., Rivkin, A., Raymond, C., Yoshikawa, M., Elkins-Tanton, L.T., Levison, H., 2018. Chapter 1 – A Brief History of Spacecraft Missions to Asteroids and Protoplanets, in: Abreu, N. (Ed.), Primitive Meteorites and Asteroids. Elsevier, Amsterdam, Oxford, Cambridge, pp. 1 – 57. doi:10.1016/B978-0-12-813325-5.00001-X.

Crusan, J., Galica, C., 2019. NASA's CubeSat Launch Initiative: Enabling broad access to space. Acta Astronautica 157, 51 – 60. doi:10.1016/j.actaastro.2018.08.048.

Dalbins, J., Janhunen, P., Noorma, M., Slavinskis, A., Presentation at the 8^{th} Interplanetary CubeSat Workshop 2019, Milan, Italy. Alternative communications approach to deep-space missions. URL: https://icubesat.org/papers/2019-2/2019-b-2-1-alternative-communications-approach-to-deep-space-missions/.

Journal Pre-proofs

Devaraj, K., Ligon, M., Blossom, E., Breu, J., Klofas, B., Colton, K., Kingsbury, R., 2019. Planet High Speed Radio: Crossing Gbps from a 3U Cubesat, in: Proc. of the 33^{rd} Annual AIAA/USU Conference on Small Satellites, Logan, UT, USA. pp. 1–10. URL: https://digitalcommons.usu.edu/smallsat/2019/all2019/106/.

Dodd, P., Shaneyfelt, M., Schwank, J., Felix, J., 2010. Current and future challenges in radiation effects on CMOS electronics. IEEE Transactions on Nuclear Science 57, 1747–1763. doi:10.1109/TNS.2010.2042613.

Duzellier, S., Nuns, T., David, J.P., Pons, C., Rey, R., Cavel, C., Chanteperdrix, G., 2018. Evaluation of tri-junction solar cells response to electrons and protons of the JUICE specific environment, in: Proc. of the 2018 IEEE 7^{th} World Conference on Photovoltaic Energy Conversion (WCPEC) (A Joint Conference of 45^{th} IEEE PVSC, 28^{th} PVSEC & 34^{th} EU PVSEC), Waikoloa Village, HI, USA. pp. 3329–3334. doi:10.1109/PVSC.2018.8548255.

EnduroSat, datasheet 2020. X-band patch antenna, viewed 16 April 2020. URL: https://www.endurosat.com/cubesat-store/all-cubesat-modules/x-band-patch-antenna/.

Envall, J., Janhunen, P., Toivanen, P., Pajusalu, M., Ilbis, E., Kalde, J., Averin, M., Kuuste, H., Laizans, K., Allik, V., et al., 2014. E-sail test payload of ESTCube-1 nanosatellite. Proceedings of the Estonian Academy of Sciences 63, 210–221. doi:10.3176/proc.2014.2S.02.

Envall, J., Toivanen, P., Janhunen, P., Presentation at the Sixth International Conference on Tethers in Space 2019, Madrid, Spain. Thin multi-wire Coulomb Drag Tether by Diffusion Bonding. URL: https://e-archivo.uc3m.es/bitstream/handle/10016/28343/SICTIS_2019.pdf?sequence=2.

ESA, open call 2016. Announcement of opportunity for new science ideas in ESA's science programme, viewed 08 April 2020. https://www.cosmos.esa.int/web/new-scientific-ideas.

ESA, technical report 2018. CDF–178(C) study report: Small Planetary Platforms (SPP) in NEO and MAB (study manager: Bayon, S.), pp. 81–100, viewed 08 April 2020. Technical Report. European Space Agency. URL: https://sci.esa.int/web/future-missions-department/-/60411-cdf-study-report-small-planetary-platforms-spp.

Evans, A., 2019. Design and Testing of the CubeSat Form Factor Thermal Control Louvers, in: Proc. of the 33^{rd} Annual AIAA/USU Conference on Small Satellites, Logan, UT, USA. p. 9. URL: https://ntrs.nasa.gov/archive/nasa/casi.ntrs.nasa.gov/20190028943.pdf.

Gibson, B.M., 2019. Miniaturized ring-down spectrometer for CubeSat-based planetary science. Applied Optics 58, 1941 – 1949. doi:10.1364/AO.58.001941.

Gilmore, D., 2002. Volume I: Fundamental technologies, in: Spacecraft Thermal Control Handbook. 2^{nd} ed.. The Aerospace Press/American Institute of Aeronautics and Astronautics, Inc, El Secundo/Resto, p. 836. doi:10.2514/4.989117.

Huang, P., Zhang, F., Chen, L., Meng, Z., Zhang, Y., Liu, Z., Hu, Y., 2018. A review of space tether in new applications. Nonlinear Dynamics 94, 1–19. doi:10.1007/s11071-018-4389-5.

Iakubivskyi, I., Janhunen, P., Praks, J., Allik, V., Bussov, K., Clayhills, B., Dalbins, J., Eenmäe, T., Ehrpais, H., Envall, J., et al., in press 2019. Coulomb drag propulsion experiments of ESTCube-2 and FORESAIL-1. Acta Astronautica (in press). doi:10.1016/j.actaastro.2019.11.030.

Imken, T., Castillo-Rogez, J., He, Y., Baker, J., Marinan, A., 2017. CubeSat flight system development for enabling deep space science, in: Proc. of the 2017 IEEE Aerospace Conference, Big Sky, MT, USA. p. 14. doi:10.1109/aero.2017.7943885.

Janhunen, P., 2011. Status report of the electric sail in 2009. Acta Astronautica 68, 567 – 570. doi:10.1016/j.actaastro.2010.02.007.

Janhunen, P., Sandroos, A., 2007. Simulation study of solar wind push on a charged wire: basis of solar wind electric sail propulsion. Annales Geophysicae 25, 755–767. doi:10.5194/angeo-25-755-2007.

Janhunen, P., Toivanen, P., Polkko, J., Merikallio, S., Salminen, P., Haeggström, E., Seppänen, H., Kurppa, R., Ukkonen, J., Kiprich, S., et al., 2010. Electric solar wind sail: Toward test missions. Review of Scientific Instruments 81, 111301. doi:10.1063/1.3514548.

Jarmak, S., Brisset, J., Colwell, J., Dove, A., Maukonen, D., Rawashdeh, S.A., Blum, J., Roe, L., 2019. CubeSat Particle Aggregation Collision Experiment (Q-PACE): Design of a 3U CubeSat mission to investigate planetesimal formation. Acta Astronautica 155, 131 – 142. doi:10.1016/j.asr.2010.10.009.

Khorenko, V., Baur, C., Siefer, G., Schachtner, M., Park, S., Boizot, B., Bourgoin, J.C., Casale, M., Campesato, R., 2017. BOL and EOL characterization of AZUR 3G LILT solar cells for ESA JUICE mission, in: Proc. of the E3S Web of Conferences Vol. 16, 11^{th} European Space Power Conference, Thessaloniki, Greece. p. 03011. doi:10.1051/e3sconf/20171603011.

Khurshid, O., Tikka, T., Praks, J., Hallikainen, M., 2014. Accommodating the plasma brake experiment on-board the Aalto-1 satellite. Proceedings of the Estonian Academy of Sciences 63, 258–266. doi:10.3176/proc.2014.2S.07.

Knuuttila, O., Kestilä, A., Kallio, E., first view 2020. Synthetic photometric landmarks used for absolute navigation near an asteroid. The Aeronautical Journal (first view), 1–20. doi:10.1017/aer.2020.41.

Journal Pre-proofs

Journal Pre-proofs

Kohout, T., Näsilä, A., Tikka, T., Granvik, M., Kestilä, A., Penttilä, A., Kuhno, J., Muinonen, K., Viherkanto, K., Kallio, E., 2018. Feasibility of asteroid exploration using CubeSats – ASPECT case study. Advances in Space Research 62, 2239 – 2244. doi:10.1016/j.asr.2019.02.011.

Krejci, D., Mier-Hicks, F., Thomas, R., Haag, T., Lozano, P., 2017. Emission Characteristics of Passively Fed Electrospray Microthrusters with Propellant Reservoirs. Journal of Spacecraft and Rockets 54, 447–458. doi:10.2514/1.A33531.

Kruijff, M., van Der Heide, E.J., 2009. Qualification and in-flight demonstration of a European tether deployment system on YES2. Acta Astronautica 64, 882–905. doi:10.1016/j.actaastro.2008.10.014.

Kulu, E., database 2020. World's largest database of nanosatellites, viewed 27 April 2020. https://www.nanosats.eu.

Kvell, U., Puusepp, M., Kaminski, F., Past, J.E., Palmer, K., Grönland, T.A., Noorma, M., 2014. Nanosatellite orbit control using MEMS cold gas thrusters. Proceedings of the Estonian Academy of Sciences 63, 279–285. doi:10.3176/proc.2014.2S.09.

Lario, D., Aran, A., Agueda, N., Sanahuja, B., 2007. Radial dependence of proton peak intensities and fluences in SEP events: Influence of the energetic particle transport parameters. Advances in Space Research 40, 289–294. doi:10.1016/j.asr.2007.01.057.

Lasagni Manghi, R., Modenini, D., Zannoni, M., Tortora, P., 2018. Preliminary orbital analysis for a CubeSat mission to the Didymos binary asteroid system. Advances in Space Research 62, 2290 – 2305. doi:10.1016/j.asr.2017.12.014.

Lätt, S., Slavinskis, A., Ilbis, E., Kvell, U., Voormansik, K., Kulu, E., Pajusalu, M., Kuuste, H., Sünter, I., et al., 2014. ESTCube-1 nanosatellite for electric solar wind sail in-orbit technology demonstration. Proceedings of the Estonian Academy of Sciences 63, 200–209. doi:10.3176/proc.2014.2S.01.

Lemmer, K., 2017. Propulsion for CubeSats. Acta Astronautica 134, 231 – 243. doi:10.1016/j.actaastro.2017.01.048.

Levin, E.M., 2007. Dynamic analysis of space tether missions, in: American Astronautical Society (AAS) Advances in the Astronautical Sciences. Univelt Incorporated, San Diego, CA, USA. volume 126, p. 462.

Li, Z., Li, J., Schmit, T.J., Wang, P., Lim, A., Li, J., Nagle, F.W., Bai, W., Otkin, J.A., Atlas, R., et al., 2019. The alternative of CubeSat-based advanced infrared and microwave sounders for high impact weather forecasting. Atmospheric and Oceanic Science Letters 12, 80–90. doi:10.1080/16742834.2019.1568816.

Journal Pre-proofs

Machuca, P., Sánchez, J., Greenland, S., 2019. Asteroid flyby opportunities using semi-autonomous CubeSats: Mission design and science opportunities. Planetary and Space Science 165, 179 – 193. doi:10.1016/j.pss.2018.11.002.

Mason, J.P., Woods, T.N., Chamberlin, P.C., Jones, A., Kohnert, R., Schwab, B., Sewell, R., Caspi, A., Moore, C.S., Palo, S., Solomon, S.C., Warren, H., 2020. MinXSS-2 CubeSat mission overview: Improvements from the successful MinXSS-1 mission. Advances in Space Research 66, 3–9. doi:10.1016/j.asr.2019.02.011.

McAdam, M.M., Rivkin, A.S., Lim, L.F., Castillo-Rogez, J., Marchis, F., Becker, T.M., 2020. Main Belt Asteroid Science in the Decade 2023-2032: Fundamental Science Questions and Recommendations on behalf of the Small Bodies Assessment Group, in: White Paper submitted to the Planetary Science Decadal Survey, pp. 1–12. URL: https://arxiv.org/abs/2007.07359.

Michel, P., Kueppers, M., Sierks, H., Carnelli, I., Cheng, A.F., Mellab, K., Granvik, M., Kestilä, A., Kohout, T., Muinonen, K., Näsilä, A., Penttila, A., Tikka, T., Tortora, P., Ciarletti, V., Hérique, A., Murdoch, N., Asphaug, E., Rivkin, A., Barnouin, O., Bagatin, A.C., Pravec, P., Richardson, D.C., Schwartz, S.R., Tsiganis, K., Ulamec, S., Karatekin, O., 2018. European component of the AIDA mission to a binary asteroid: Characterization and interpretation of the impact of the DART mission. Advances in Space Research 62, 2261 – 2272. doi:10.1016/j.asr.2017.12.020.

Nascetti, A., Mirasoli, M., Marchegiani, E., Zangheri, M., Costantini, F., Porchetta, A., Iannascoli, L., Lovecchio, N., Caputo, D., de Cesare, G., Pirrotta, S., Roda, A., 2019. Integrated chemiluminescence-based lab-on-chip for detection of life markers in extraterrestrial environments. Biosensors and Bioelectronics 123, 195 – 203. doi:10.1016/j.bios.2018.08.056.

Nohmi, M., 2009. Initial experimental result of pico-satellite KUKAI on orbit, in: Proc. of the 2009 International Conference on Mechatronics and Automation, Changchun, China. pp. 2946–2951. doi:10.1109/ICMA.2009.5246063.

Oleynik, P., Vainio, R., Hedman, H.P., Punkkinen, A., Punkkinen, R., Salomaa, L., Säntti, T., Tuominen, J., Virtanen, P., Bosser, A., Janhunen, P., Kilpua, E., Palmroth, M., Praks, J., Slavinskis, A., Kakakhel, S.R., Peltonen, J., Plosila, J., Tammi, J., Tenhunen, H., Westerlund, T., 2020. Particle Telescope aboard FORESAIL-1: Simulated performance. Advances in Space Research 66, 29 – 41. doi:10.1016/j.asr.2019.11.010.

Pajusalu, M., Slavinskis, A., 2019. Characterization of Asteroids Using Nanospacecraft Flybys and Simultaneous Localization and Mapping, in: Proc. of the 2019 IEEE Aerospace Conference, Big Sky, MT, USA. p. 9. doi:10.1109/AERO.2019.8741921.

Journal Pre-proofs

Palmroth, M., Praks, J., Vainio, R., Janhunen, P., Kilpua, E.K.J., Afanasiev, A., Ala-Lahti, M., Alho, A., Asikainen, T., Asvestari, E., Battarbee, M., Binios, A., Bosser, A., Brito, T., Dubart, M., Envall, J., et al., 2019. FORESAIL-1 CubeSat Mission to Measure Radiation Belt Losses and Demonstrate Deorbiting. Journal of Geophysical Research: Space Physics 124, 5783–5799. doi:10.1029/2018JA026354.

Palomba, E., Shea, M., 2018. Preface: Past, present and future of small body science and exploration. Advances in Space Research 62, 1919 – 1920. doi:10.1016/j.asr.2018.08.031.

Poghosyan, A., Golkar, A., 2017. CubeSat evolution: Analyzing CubeSat capabilities for conducting science missions. Progress in Aerospace Sciences 88, 59 – 83. doi:10.1016/j.paerosci.2016.11.002.

Rose, R., Dickinson, J., Ridley, A., 2012. CubeSats to NanoSats; Bridging the gap between educational tools and science workhorses, in: Proc. of the 2012 IEEE Aerospace Conference, Big Sky, MT, USA. p. 11. doi:10.1109/AERO.2012.6187417.

Schoolcraft, J., Klesh, A., Werne, T., 2017. MarCO: Interplanetary Mission Development on a CubeSat Scale, in: Cruzen, C., Schmidhuber, M., Lee, Y.H., Kim, B. (Eds.), Space Operations: Contributions from the Global Community. Springer, Cham, pp. 221–231. doi:10.1007/978-3-319-51941-8_10.

Segret, B., Hestroffer, D., Quinsac, G., Agnan, M., Vannitsen, J., Mosser, B., 2018. In-flight orbit determination for a deep space CubeSat, in: Proc. of the 2018 IEEE Aerospace Conference, Big Sky, MT, USA. p. 12. doi:10.1109/AERO.2018.8396756.

Selčan, D., Kirbiš, G., Kramberger, I., 2017. Nanosatellites in LEO and beyond: Advanced Radiation protection techniques for COTS-based spacecraft. Acta Astronautica 131, 131 – 144. doi:10.1016/j.actaastro.2016.11.032.

Seppänen, H., Kiprich, S., Kurppa, R., Janhunen, P., Hæggström, E., 2011. Wire-to-wire bonding of μm-diameter aluminum wires for the Electric Solar Wind Sail. Microelectronic Engineering 88, 3267–3269. doi:10.1016/j.mee.2011.07.002.

Seppänen, H., Rauhala, T., Kiprich, S., Ukkonen, J., Simonsson, M., Kurppa, R., Janhunen, P., Hæggström, E., 2013. One kilometer (1 km) electric solar wind sail tether produced automatically. Review of Scientific Instruments 84, 095102. doi:10.1063/1.4819795.

Singhal, N., Levchenko, I., Huang, S., Xu, L., Potrivitu, G.C., Cherkun, O., Fang, J., Bazaka, K., Xu, S., 2019. 3D-Printed Multilayered Reinforced Material System for Gas Supply in CubeSats and Small Satellites. Advanced Engineering Materials 21, 1900401. doi:10.1002/adem.201900401.

Journal Pre-proofs

Journal Pre-proofs

Sinha, R.S., Wei, Y., Hwang, S.H., 2017. A survey on LPWA technology: LoRa and NB-IoT. ICT Express 3, 14 – 21. doi:10.1016/j.icte.2017.03.004.

Slavinskis, A., Iakubivskyi, I., Janhunen, P., Toivanen, P., Muinonen, K., Penttilä, A., Granvik, M., Kohout, T., Gritsevich, M., Pajusalu, M., Sünter, I., et al., 2018. Nanospacecraft fleet for multi-asteroid touring with electric solar wind sails, in: Proc. of the 2018 IEEE Aerospace Conference, Big Sky, MT, USA. p. 20. doi:10.1109/AERO.2018.8396670.

Slavinskis, A., Kulu, E., Viru, J., Valner, R., Ehrpais, H., Uiboupin, T., Järve, M., Soolo, E., Envall, J., Scheffler, T., et al., 2014. Attitude determination and control for centrifugal tether deployment on the ESTCube-1 nanosatellite. Proceedings of the Estonian Academy of Sciences 63, 242–249. doi:10.3176/proc.2014.2S.05.

Slavinskis, A., Pajusalu, M., Kuuste, H., Ilbis, E., Eenmäe, T., Sünter, I., Laizans, K., Ehrpais, H., Liias, P., Kulu, E., et al., 2015. ESTCube-1 in-orbit experience and lessons learned. IEEE Aerospace and Electronic Systems Magazine 30, 12–22. doi:10.1109/MAES.2015.150034.

Snodgrass, C., Jones, G., Boehnhardt, H., Gibbings, A., Homeister, M., Andre, N., Beck, P., Bentley, M., Bertini, I., Bowles, N., et al., 2018. The Castalia mission to Main Belt Comet 133P/Elst-Pizarro. Advances in Space Research 62, 1947 – 1976. doi:10.1016/j.asr.2017.09.011.

Stone, N., Raitt, W., Wright, K., 1999. The TSS-1R electrodynamic tether experiment: Scientific and technological results. Advances in Space Research 24, 1037 – 1045. doi:10.1016/S0273-1177(99)00551-7.

Swartz, W.H., Lorentz, S.R., Huang, P.M., Reilly, S.M., Reilly, N.M., Papadakis, S.J., 2019. Radiometer Assessment Using Vertically Aligned Nanotubes (RAVAN), in: Proc. of the IGARSS 2019 – 2019 IEEE International Geoscience and Remote Sensing Symposium, Yokohama, Japan. pp. 4975–4977. doi:10.1109/IGARSS.2019.8899776.

Sznajder, M., Geppert, U., Dudek, M.R., 2018. Hydrogen blistering under extreme radiation conditions. npj Materials Degradation 2, 1–8. doi:10.1038/s41529-017-0024-z.

Toivanen, P., Janhunen, P., 2012. Spin Plane Control and Thrust Vectoring of Electric Solar Wind Sail. Journal of Propulsion and Power 29, 178–185. doi:10.2514/1.B34330.

Toivanen, P., Janhunen, P., 2014. Electric Solar Wind Sail: Deployment, Long-Term Dynamics, and Control Hardware Requirements, in: Macdonald, M. (Ed.), Advances in Solar Sailing. Springer, Berlin, Heidelberg, pp. 977–987. doi:10.1007/978-3-642-34907-2_58.

Journal Pre-proofs

Tullino, S.K., Swenson, E.D., 2017. Testing and Evaluating Deployment Profiles of the Canisterized Satellite Dispenser (CSD), in: Proc. of the 55^{th} AIAA Aerospace Sciences Meeting, Grapevine, Texas, USA. doi:10.2514/6.2017-0850.

Walker, R., Binns, D., Bramanti, C., Casasco, M., Concari, P., Izzo, D., Feili, D., Fernandez, P., Fernandez, J.G., Hager, P., Koschny, D., Pesquita, V., Wallace, N., Carnelli, I., Khan, M., Scoubeau, M., Taubert, D., 2018. Deep-space CubeSats: thinking inside the box. Astronomy & Geophysics 59, 24–30. doi:10.1093/astrogeo/aty232.

Woellert, K., Ehrenfreund, P., Ricco, A.J., Hertzfeld, H., 2011. Cubesats: Cost-effective science and technology platforms for emerging and developing nations. Advances in Space Research 47, 663 – 684. doi:10.1016/j.asr.2010.10.009.

Yekan, T., Baktur, R., Swenson, C., Shaw, H., Kegege, O., Presentation at the 32^{nd} Annual AIAA/USU Conference on Small Satellites 2018, Logan, UT, USA. Integrated Solar-Panel Antenna Array for CubeSats. URL: https://ntrs.nasa.gov/archive/nasa/casi.ntrs.nasa.gov/20180007309.pdf.

Yu, B.S., Wen, H., Jin, D.P., 2018. Review of deployment technology for tethered satellite systems. Acta Mechanica Sinica 34, 754–768. doi:10.1007/s10409-018-0752-5.

Zacny, K., Metzger, P., Luczek, K., Mantovani, J., Mueller, R.P., Spring, J., 2016. The World is Not Enough (WINE): Harvesting Local Resources for Eternal Exploration of Space, in: Proc. of the AIAA SPACE 2016, In-Situ Resource Utilization, Long Beach, CA, USA. p. 20. doi:10.2514/6.2016-5279.

Journal Pre-proofs